Cell Reports

Resource

A spatial and projection-based transcriptomic atlas of paraventricular hypothalamic cell types

Graphical abstract

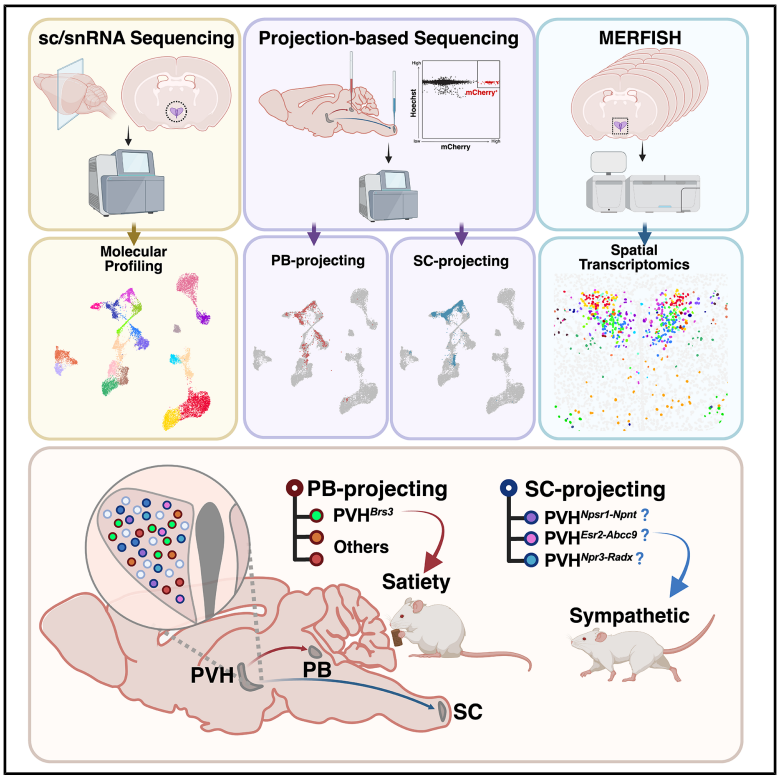

Highlights

- Spatial transcriptomic characterization of neurons from the PVH and surrounding areas
- Distinct transcriptional programs define neuroendocrine and centrally projecting PVH neurons
- Projection-based snRNA-seq reveals putative PVH regulators of sympathetic drive and feeding
- PVH^{Brs3} neurons regulate body weight and reduce feeding via projections to the parabrachial

Authors

Yuxi Li, Trevor C. Butler, Stefano Nardone, ..., Linus T. Tsai, Bradford B. Lowell, Jon M. Resch

Correspondence

ltsai@bidmc.harvard.edu (L.T.T.), blowell@bidmc.harvard.edu (B.B.L.), jon-resch@uiowa.edu (J.M.R.)

In brief

Li et al. present a spatial transcriptomic atlas of the mouse paraventricular hypothalamus (PVH) and provide molecular markers for parabrachial- and spinal cord-projecting PVH populations. They further show that *Brs3*-expressing PVH neurons regulate satiety, as they co-express *Mc4r*, cause weight gain when silenced, and reduce food intake via parabrachial projections.

Li et al., 2026, Cell Reports *45*, 116904
February 24, 2026
https://doi.org/10.1016/j.celrep.2025.116904

CellPress

Cell Reports

CellPress
OPEN ACCESS

Resource

A spatial and projection-based transcriptomic atlas of paraventricular hypothalamic cell types

Yuxi Li,[1,9] Trevor C. Butler,[1,9] Stefano Nardone,[2] Christopher L. Jacobs,[2,4] Amelia M. Douglass,[2,8] Joseph C. Madara,[2] Miriam C. McDonough,[1] Jenkang Tao,[2] Elijah D. Lowenstein,[2] Luhong Wang,[2] Deepti Pant,[2] Samuel J. Walker,[2] Annette Wang,[2] Harini Srinivasan,[2] Zongfang Yang,[2] John N. Campbell,[3] Linus T. Tsai,[2,4,*] Bradford B. Lowell,[2,5,*] and Jon M. Resch[1,6,7,10,*]

[1]Department of Neuroscience and Pharmacology, Carver College of Medicine, University of Iowa, Iowa City, IA, USA
[2]Division of Endocrinology, Diabetes, and Metabolism, Department of Medicine, Beth Israel Deaconess Medical Center, Harvard Medical School, Boston, MA, USA
[3]Department of Biology, University of Virginia, Charlottesville, VA, USA
[4]Broad Institute of MIT and Harvard, Cambridge, MA, USA
[5]Program in Neuroscience, Harvard Medical School, Boston, MA, USA
[6]Iowa Neuroscience Institute, University of Iowa, Iowa City, IA, USA
[7]Fraternal Order of Eagles Diabetes Research Center, Carver College of Medicine, University of Iowa, Iowa City, IA, USA
[8]Present address: Institute of Science and Technology Austria, Klosterneuburg, Austria
[9]These authors contributed equally
[10]Lead contact
*Correspondence: ltsai@bidmc.harvard.edu (L.T.T.), blowell@bidmc.harvard.edu (B.B.L.), jon-resch@uiowa.edu (J.M.R.)
https://doi.org/10.1016/j.celrep.2025.116904

SUMMARY

The paraventricular hypothalamus (PVH) controls behavioral and physiologic processes, including appetite, social behavior, autonomic outflow, and pituitary hormone secretion. However, molecular markers for centrally projecting PVH neuron populations remain largely undefined, and a complete census of PVH cell types has not been established. Therefore, we performed extensive single-cell/nucleus RNA sequencing to catalog PVH neuron subtypes and multiplexed error-robust fluorescence *in situ* hybridization (MERFISH) to map them spatially. Our spatial transcriptomic atlas resolves 26 *Sim1*$^{+}$ and 29 GABAergic neuron populations from the PVH and surrounding areas. Additionally, projection-based profiling identified neurons that project to the parabrachial region (PB) and spinal cord, helping to determine PVH populations that regulate satiety and sympathetic nervous system activity, respectively. Notably, activation of PB-projecting PVH neurons expressing *Brs3* reduces food intake, and silencing them causes obesity. Together, this atlas contributes high-resolution PVH spatial and circuit-based gene expression profiles, representing a valuable resource for the field of homeostasis.

INTRODUCTION

The paraventricular hypothalamus (PVH) is among the most functionally diverse and anatomically complex regions of the brain. Essential for maintaining homeostasis, the PVH integrates information about the internal state and external environment and accordingly adapts endocrine, autonomic, and behavioral outputs.[1–3] PVH neurons are typically classified based on cytoarchitectural subdivisions, projections, and neuroendocrine hormone expression.[1–9] PVH parvicellular neuron projections to the median eminence release hormones into the hypophyseal portal system that then cause release of anterior pituitary hormones to regulate the stress response, thyroid function, and growth, whereas PVH magnocellular neuron projections to the posterior pituitary release vasopressin and oxytocin directly into the systemic circulation.[1,3] Centrally projecting PVH neurons, on the other hand, are a highly heterogeneous and poorly defined class of PVH neurons innervating regions of the hypothalamus, midbrain, hindbrain, and spinal cord to mediate autonomic and behavioral responses.[10] Despite their importance, the molecular and functional diversity of centrally projecting PVH neurons remains unresolved.

Among their many functions, centrally projecting PVH neurons are well known for regulating energy balance. PVH neurons that express the melanocortin 4 receptor (*Mc4r*) are crucial for body weight control as their activation reduces food intake, while loss of function causes hyperphagia and obesity.[11–15] Notably, several other PVH neurons have been reported to decrease food intake,[15–21] including prodynorphin (*Pdyn*)-expressing neurons, which, like PVH^{Mc4r} neurons, regulate feeding behavior via projections to the parabrachial region (PB). These two populations are distinct, however, because their simultaneous inhibition causes additive effects on hyperphagia and obesity.[12,21] In contrast, the PVH oppositely regulates feeding behavior via neurons expressing thyrotropin-releasing hormone (*Trh*) and pituitary adenylate cyclase-activating peptide (*Adcyap1*) that induce

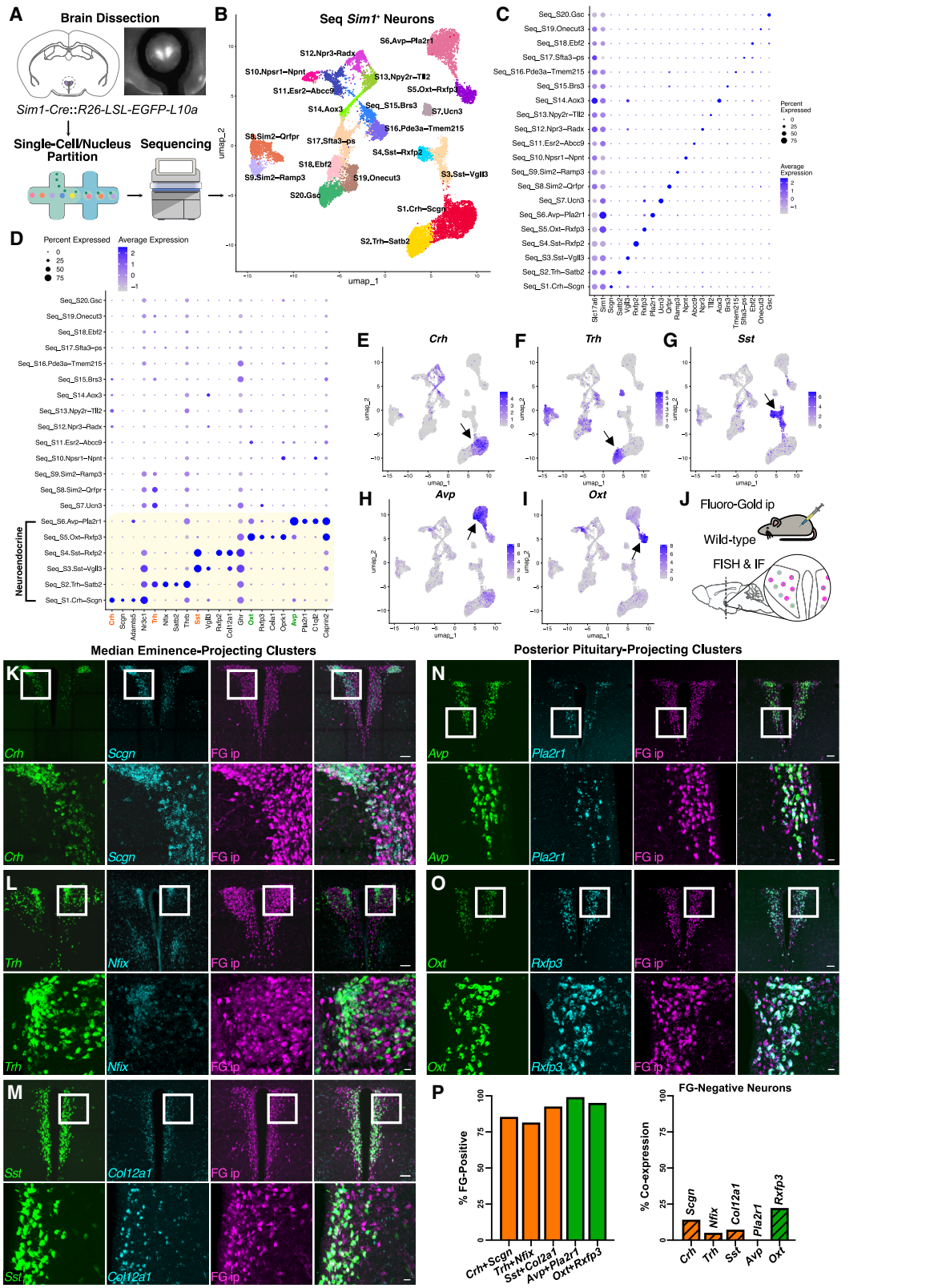

(legend on next page)

hunger through activation of agouti-related peptide (AgRP) neurons in the arcuate nucleus (ARC),[22] highlighting the complexity of appetite regulation by the PVH. Besides appetite, the PVH also controls energy expenditure through nitric oxide synthase 1 (*Nos1*)- and brain-derived neurotrophic factor (*Bdnf*)-expressing neuron projections to the spinal cord that drive sympathetic nervous system output to adipose tissue.[19,23,24] That said, because these previously described genetic markers are expressed across multiple PVH neuron subpopulations, the exact transcriptional identity of energy balance-regulating neurons remains unclear, and the lack of precise markers limits our ability to study their regulation and function selectively.

Recent studies characterizing PVH neurons at the molecular level represent an important step toward understanding the diversity of cell types present.[25–27] However, the power of these studies has been limited by sample size and the inability to resolve their spatial organization. Moreover, large-scale single-cell and spatial transcriptomic studies of the entire mouse brain[28–31] or hypothalamus[32] lack detailed analysis of PVH neuron subtypes, leaving significant gaps in our understanding of the molecular heterogeneity of PVH neurons. To address these limitations, we employed single-cell/nucleus RNA sequencing (sc/snRNA-seq) and multiplexed error-robust fluorescence *in situ* hybridization (MERFISH) to generate a comprehensive spatial transcriptomic atlas of the PVH at single-cell resolution. Further, we sequenced spinal cord- and PB-projecting PVH neurons to identify marker genes for neurons controlling sympathetic nervous system activity and feeding behavior, respectively. Leveraging this information, we show that stimulation of bombesin-like receptor 3 (*Brs3*)-expressing PVH neuron projections to the PB reduces food intake, PVH^{Brs3} neurons are downstream of AgRP neurons, and their silencing promotes weight gain.

RESULTS

Molecular profiling of the PVH

To classify PVH cell types based on their genome-wide expression patterns, we performed single-cell RNA-seq using Drop-seq[33] and single-nucleus RNA-seq using DroNc-seq[34] and the 10X Chromium platform on adult male and female mice (Figures S1A and S1B). For each approach, we micro-dissected the PVH region from *Sim1*-Cre[14]::L10-GFP[22] or wild-type mice (Figure 1A). After sc/snRNA-seq, analyses were performed using Seurat version 5,[35,36] integrating by sequencing run ("batch"), to generate an atlas of 42,948 cells/nuclei from the PVH and immediately surrounding regions. Cell-type clusters were visualized with uniform manifold approximation and projection (UMAP) and annotated using canonical cell-type marker genes previously reported in the literature, revealing nearly 80% neurons, with the remaining cells forming distinct populations of non-neuronal/glial cells (Figures S1C–S1E; Table S1). We next examined the effects of sc/snRNA-seq technology and sex on cell clustering. While gene and cell type detection differed somewhat between the droplet-based sc/snRNA-seq methods, cells/nuclei from both sexes and all technologies were represented in all clusters (Figures S1F–S1I).

To gain specific insight into PVH neuron diversity, we next re-clustered 33,644 neuronal cells/nuclei, which produced a UMAP with clusters predominantly segregated into inhibitory neurons expressing the vesicular GABA transporter (*Slc32a1*; VGAT) and excitatory neurons expressing the vesicular glutamate transporter 2 (*Slc17a6*; VGLUT2; Figures S2A–D, S2G, and S2H; Table S2A). We also observed further segregation of excitatory neurons into those expressing the PVH marker gene *Sim1* or the thalamic marker gene *Tcf7l2* (Figures S2B, S2E, S2F, S2I, and S2J). Histological assessment confirmed that *Slc32a1* is expressed primarily in areas surrounding the PVH,[37,38] *Sim1* is predominantly expressed within the PVH,[39] and *Tcf7l2* expression is constrained to thalamus dorsal to the PVH.[31,40] We subsequently re-clustered glutamatergic and GABAergic neurons separately, resulting in 22 excitatory clusters from 18,920 glutamatergic cells/nuclei (Figures S2K and S2L; Table S2B) and 28 inhibitory populations from 13,075 GABAergic cells/nuclei surrounding the PVH (Figures S2M and S2N; Table S2C). Finally, to specifically investigate PVH neuron gene expression profiles, we re-clustered only neurons from *Sim1*-positive populations. At this point, we also sought to take advantage of publicly available data. To do so, we examined PVH-assigned cells from the "HypoMap" study, an integrated reference atlas of the entire mouse hypothalamus (Figures S3A–S3F; Table S3A).[32] However, after integrating 5,119 putative PVH neurons expressing *Sim1* from HypoMap with our study, we observed discrepancies between the datasets (Figures S3G–S3I; Table S3B). Notably, seven *Sim1*$^+$ clusters comprised almost entirely neurons from this study (Figure S3J), and a large proportion of HypoMap neurons express markers for neurons adjacent to the PVH ("peri-PVH"), including *Cabp7*, *Onecut3*,[41] and *Gsc*[42] (Figure S3K). These results suggest that there is inadequate representation of PVH

Figure 1. Single-cell/nucleus transcriptional profiling of *Sim1*$^+$ neurons

(A) Illustration of sc/snRNA-seq workflow.

(B) *Sim1*$^+$ UMAP comprised 16,598 cells/nuclei.

(C) Dot plot showing the expression of *Slc17a6*, *Sim1*, and marker genes for *Sim1*$^+$ clusters.

(D) Dot plot showing the expression of top marker genes for neuroendocrine clusters.

(E–I) Feature plots depicting the expression of *Crh* (E), *Trh* (F), *Sst* (G), *Avp* (H), and *Oxt* (I).

(J) Experimental schematic for retrograde labeling of neuroendocrine neurons with intraperitoneal (ip) injections of Fluoro-Gold (FG) together with fluorescent *in situ* hybridization (FISH) for top neuroendocrine marker genes.

(K–O) Immunofluorescence (IF) for ip-injected FG and FISH of marker genes of neuroendocrine clusters at representative bregma levels. Median eminence-projecting (left): *Crh* and *Scgn* (∼−0.7 mm from bregma) (K), *Trh* and *Nfix* (∼−0.8 mm from bregma) (L), and *Sst* and *Col12a1* (∼−0.5 mm from bregma) (M). Posterior pituitary-projecting (right): *Avp* and *Pla2r1* (∼−0.7 mm from bregma) (N) and *Oxt* and *Rxfp3* (∼−0.7 mm from bregma) (O). The lower panels represent magnified views of the boxed regions highlighted in the upper panels.

(P) Percentage of neurons that co-express distinct neuroendocrine gene pairs that are also labeled by ip-injected FG (left) and percentage of FG-negative neurons that co-express neuroendocrine marker gene pairs (right). Low-magnification scale bar, 100 μm, high-magnification scale bar, 20 μm.

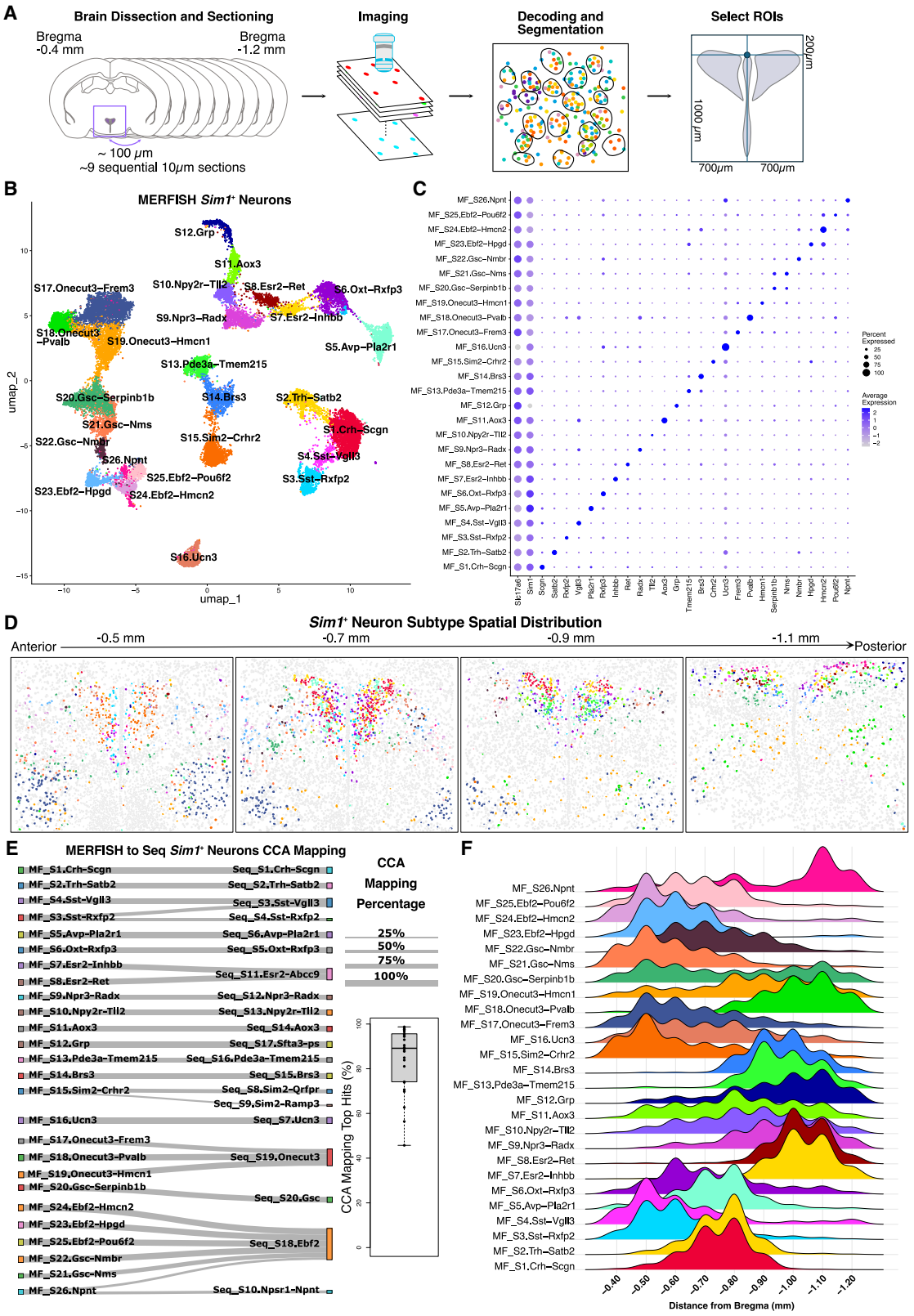

(legend on next page)

neuron subtypes within the HypoMap study.[32] Thus, we instead integrated *Sim1*$^{+}$ PVH neurons from the Allen Brain Cell (ABC) Atlas,[29] resulting in 9,301 *Sim1*$^{+}$ neurons from this study and 7,297 from the ABC Atlas. Analysis after integration identified 20 distinct clusters, each consisting of cells from both studies that we annotated based on the expression of one or more marker genes (Figures 1B, 1C, and S3L–S3N; Table S4). This final sc/snRNA-seq atlas, comprising 16,598 *Sim1*$^{+}$ neurons, greatly surpasses the number of cells previously available from single-cell transcriptomic studies of the PVH.

Transcriptional profiles of PVH neuroendocrine populations revealed by sc/snRNA-seq

The PVH is home to parvicellular and magnocellular neuroendocrine neurons that are defined by the synthesis and release of one of five well-known hormones, which include corticotropin-releasing hormone (*Crh*), thyrotropin-releasing hormone (*Trh*), somatostatin (*Sst*), arginine vasopressin (*Avp*), and oxytocin (*Oxt*).[1] In this study, we identified distinct *Sim1*$^{+}$ neuronal clusters that are enriched for these genes annotated as Seq_S1.Crh-Scgn, Seq_S2.Trh-Satb2, Seq_S3.Sst-Vgll3, Seq_S4.Sst-Rxfp2, Seq_S5.Oxt-Rxfp3, and Seq_S6.Avp-Pla2r1 (Figures 1D–1I) and hypothesized that these clusters represent the PVH neuroendocrine populations. However, since these pituitary-regulating hormone genes are expressed across multiple PVH neuron clusters, we sought to confirm our neuroendocrine cluster classifications. To label median eminence- and posterior pituitary-projecting PVH neurons, C57BL/6J mice received intraperitoneal (ip) injections of the retrograde tracer Fluoro-Gold, which labels neurons that project outside the blood-brain barrier when administered systemically (Figure 1J).[1,43,44] We then performed co-labeling studies for each putative neuroendocrine cluster using fluorescence *in situ* hybridization (FISH) to demonstrate co-expression of neuroendocrine hormones with marker genes determined by sc/snRNA-seq, followed by immunofluorescence for Fluoro-Gold. Of note, sc/snRNA-seq identified two putative PVH neuroendocrine populations that express *Sst*, Seq_S3.Sst-Vgll3 and Seq_S4.Sst-Rxfp2, the significance of which is unknown, as each expresses the growth hormone receptor (*Ghr*), likely to facilitate negative feedback.[45] To assess the neuroendocrine identity of these PVH^{Sst} neuron clusters, we performed FISH for *Col12a1,* taking advantage of its enrichment in both clusters (Figure 1D). Other gene pairs tested were *Crh-Scgn*, *Trh-Nfix*, *Oxt-Rxfp3*, and *Avp-Pla2r1*. In all cases, greater than 80% of neurons co-expressing a neuroendocrine peptide and its corresponding marker gene were also positive for Fluoro-Gold (Figures 1K–1P). Furthermore, Fluoro-Gold negative neurons expressing *Crh*, *Trh*, *Sst*, *Avp*, and *Oxt* rarely co-expressed the corresponding neuroendocrine marker gene determined by sc/snRNA-seq (Figure 1P). These findings confirm our neuroendocrine classifications and demonstrate that the intersection of neuroendocrine marker gene pairs identified by sc/snRNA-seq enables approaches for gaining selective genetic access to pituitary-regulating PVH neuron populations.

Given that neuroendocrine neurons share a common projection target and release large amounts of neuropeptide hormones into the circulation, we next assessed whether we could identify a shared transcriptional program that differentiates them from centrally projecting neurons. Marker gene analysis revealed a sharp division in transcriptional profiles (Figures S4A and S4B; Tables S5A and S5B), identifying genes that distinguish neuroendocrine populations (e.g., *Creb3l2*; Figures S4C and S4E) and centrally projecting neurons (e.g., *Ntng1*; Figures S4D and S4E). To further characterize these transcriptional differences, we performed Gene Ontology (GO) enrichment analysis on genes upregulated in PVH neuroendocrine and centrally projecting populations (Figures S4F and S4G; Tables S5C and S5D). We found neuroendocrine neurons are most significantly enriched for genes related to ribosomal function and translation, which may be crucial for the synthesis of large quantities of neuropeptides. In contrast, centrally projecting neurons were strongly enriched for genes related to the formation and regulation of synapses. Additional marker gene analysis comparing median eminence-projecting and posterior pituitary-projecting neuroendocrine subtypes also demonstrated transcriptional differences, highlighting *Agtr1a* as a marker for median eminence-projecting (parvicellular) neurons and *Plekhg1* as a marker for posterior pituitary-projecting (magnocellular) neurons (Figures S4H–S4L; Tables S5E and S5F). GO enrichment analysis revealed that the top pathways for median eminence-projecting populations are related to ion channel activity (Figure S4M; Table S5G). Meanwhile, posterior pituitary-projecting populations again showed enrichment for ribosomal function and translation-related pathways, which likely are critical for supporting direct secretion of large quantities of AVP and OXT into the systemic circulation to regulate distant target organs (Figure S4N; Table S5H).[1]

Spatial transcriptomic profiling of the PVH with MERFISH

Droplet-based sc/snRNA-seq technologies are powerful tools for identifying and characterizing cell type diversity. However, they require tissue dissociation, preventing the retention of spatial information, and may fail to detect functionally

Figure 2. MERFISH spatial transcriptomic profiles of *Sim1*$^{+}$ neurons in the PVH

(A) Schematic showing key steps in the MERFISH experimental workflow.

(B) UMAP showing 24,132 *Sim1*$^{+}$ neurons.

(C) Dot plot showing the expression of *Slc17a6, Sim1,* and marker genes for *Sim1*$^{+}$ MERFISH clusters.

(D) Representative coronal MERFISH sections show the spatial distribution of *Sim1*$^{+}$ neuron types from a male mouse (Slide 3), color-coded by cluster identity.

(E) Sankey plot depicting cluster correspondence between MERFISH *Sim1*$^{+}$ neuron clusters and sc/snRNA-seq *Sim1*$^{+}$ neuron clusters in the PVH (25% cutoff). Line thickness represents the proportion of cells from each MERFISH cluster that is predicted to map to a particular sc/snRNA-seq cluster. Box and whisker plot (right) depicts the upper and lower quartiles of the canonical correlation analysis (CCA) mapping percentages for the top hit from each MERFISH cluster. The black line within the box represents the median CCA mapping percentage, and the whiskers depict min/max values within 1.5 times the interquartile range.

(F) Ridge plot showing the distribution of *Sim1*$^{+}$ neuron clusters along the rostral-to-caudal axis.

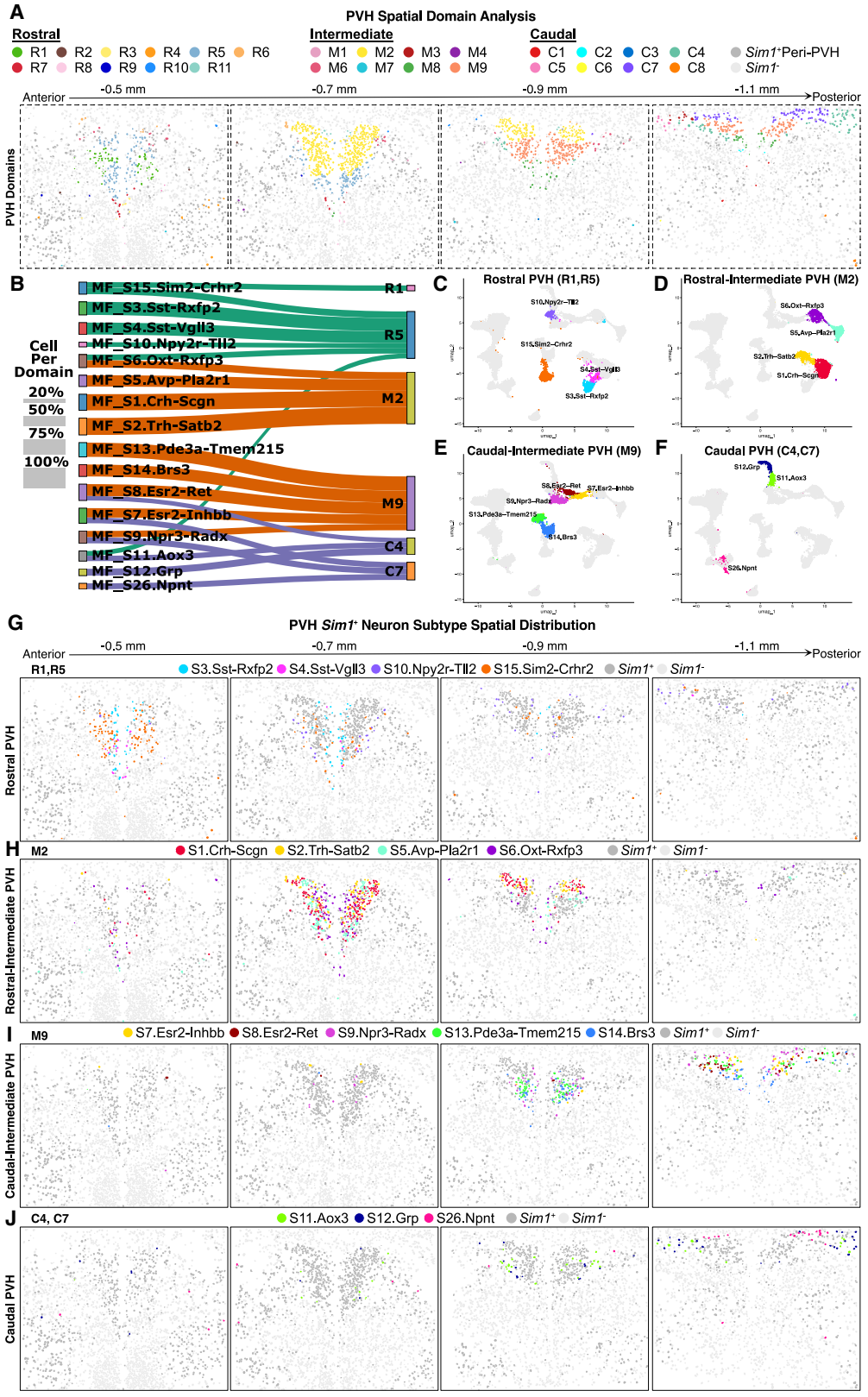

(legend on next page)

important genes expressed at low levels. Therefore, we used MERSCOPE,[29,46] an imaging-based MERFISH platform capable of detecting low-abundance transcripts with single-molecule sensitivity,[46–48] to resolve the spatial organization of the PVH and surrounding regions. We assayed the spatial distribution of 503 genes specifically curated for the PVH region, comprised of top differentially expressed genes identified in our sc/snRNA-seq analyses, canonical marker genes for neuronal and glial populations, and functionally relevant genes selected from the literature (Tables S6A and S6B). In total, we imaged 41 coronal sections across six mice. Brain sections were collected at intervals of approximately 100 μm along the rostral-caudal axis of the PVH, ranging from approximately 0.4 to 1.2 mm caudal to bregma according to the Franklin-Paxinos atlas.[49] After imaging, individual cells were segmented using Cellpose 2.0[50] and filtered to remove cells with low transcript counts (Figure S5A). Then, for each coronal slice, we systematically defined the region of interest (ROI) covering the PVH and peri-PVH and subset the data to retain only cells within these regions (Figure 2A; Table S6C). After subsetting for the ROI, we were able to perform cell type clustering on 155,546 spatially resolved cells. Our initial all-cell MERFISH clustering comprised eight major cell types, approximately 65% of which were classified as neurons (Figures S5B–S5D; Table S7A). Each MERFISH slide contributed proportionally to all major cell type clusters, with no sex-dependent batch effects on clustering observed after data integration, demonstrating the technical replicability of the MERFISH assay across multiple trials (Figures S5E and S5F). Importantly, plotting our MERFISH spatial data using polygons color-coded by major cell type, with neurons divided into excitatory and inhibitory populations, recapitulates the known cellular organization in this region of the hypothalamus (Figures S5G and S5H).

Following initial all-cell MERFISH analysis, we performed subclustering of excitatory (*Slc17a6*$^+$) and inhibitory (*Slc32a1*$^+$) neurons as we did for sc/snRNA-seq data. Excitatory neurons were further divided based on *Sim1* expression, and the three major neuron types, *Slc17a6*$^+$/*Sim1*$^+$, *Slc17a6*$^+$/*Sim1*$^-$ (Figures S5I and S5J; Table S7B), and *Slc32a1*$^+$, were reclustered. To characterize the anatomical location of MERFISH cell types, we next performed spatial domain analysis on all neuron subpopulations using the SpaDo package in R.[51] This computational method integrates gene expression and spatial proximity information from multiple slices, allowing for unbiased anatomical categorization of neurons, which can be used to link the molecular profiles from MERFISH cell types to previously described neuroanatomical PVH subdivisions.[1] Twenty-nine domains were identified distributed across "Rostral" (R1–R11; −0.4 to −0.6 mm from bregma), "Intermediate" (M1–M9; −0.7 to −0.9 mm from bregma), and "Caudal" (C1–C9; −1.0 to −1.2 mm from bregma) regions (Figures S6A and S6B; Table S8A). Finally, the majority of spatial domains show neuron subtype enrichment, with domains R4, R5, M1, M2, M9, C4, and C7 primarily encompassing *Slc17a6*$^+$/*Sim1*$^+$ neurons (Figure S6C; Table S8B).

Spatial distribution of *Sim1*$^+$ MERFISH clusters

MERFISH cell clustering of 24,132 *Sim1*-expressing neurons resulted in the identification of 26 glutamatergic (*Slc17a6*$^+$) clusters that we annotated according to the expression of one or more marker genes (Figures 2B and 2C; Table S9A). Importantly, plotting *Sim1* expression and *Sim1*$^+$ MERFISH clusters confirms the expected spatial enrichment within the PVH (Figures 2D and S6D).[31,39] Next, we performed canonical correlation analysis (CCA) to examine the transcriptional similarity between MERFISH-defined and sc/snRNA-seq-defined *Sim1*$^+$ clusters.[36] CCA identified strong correspondence between cells belonging to MERFISH *Sim1*$^+$ clusters and those from *Sim1*$^+$ sc/snRNA-seq (Figure 2E; Table S9B). There are, however, a few instances where multiple MERFISH *Sim1*$^+$ clusters map to a single sc/snRNA-seq cluster. For example, all MERFISH clusters enriched for *Onecut3*, including MF_S17.Onecut3-Frem3, MF_S18.Onecut3-Pvalb, and MF_S19.Onecut3-Hmcn1 (Figure S6E), map to the Seq_S15.Onecut3 cluster. We hypothesize that this is due to the improved gene detection with MERFISH, which increased our resolution of neurons enriched for *Onecut3* expression and produced multiple clusters upon analysis. Overall, there is a general correspondence between *Sim1*$^+$ MERFISH and sc/snRNA-seq clusters, enabling the inference of genome-wide expression levels for spatially resolved neuron populations in the PVH region.

We next evaluated the spatial location of *Sim1*$^+$ clusters from rostral to caudal (Figure 2F). Using the multi-slice spatial domain analysis performed on all neurons above (Figures S6A–S6C), we delineated PVH and "peri-PVH" *Sim1*$^+$ neuron compartments (Figures 3A, 3B, S8A, and S8C), and PVH neurons were further partitioned into "Rostral," "Rostral-Intermediate," "Caudal-Intermediate," and "Caudal" spatial groups (Figures 3C–3J). The Rostral PVH clusters include MF_S3.Sst-Rxfp2, MF_S4.Sst-Vgll3, MF_S10.Npy2r-Tll2, and MF_S15.Sim2-Crhr2, which are primarily located in spatial domains R1 and R5, approximating, respectively, the anterior parvicellular (PVHap) and anterior periventricular (PVHpv) parts of the PVH (Figures 3A–3C and 3G).[1] As expected, *Sst*$^+$ neurons are concentrated in the PVHpv, while MF_S10.Npy2r-Tll2 and MF_S15.Sim2-Crhr2 are located in the PVHap. Of interest, single-minded 2 (*Sim2*), a homolog of *Sim1*, marks the MF_S15.Sim2-Crhr2 cluster (Figures S7A–S7E) and MF_S18.Onecut3-Pvalb clusters, the latter of which is located in the caudal ventrolateral peri-PVH region (Figures S7D and S8B). Notably, PVH^{Sim2} neurons are not labeled by systemic Fluoro-Gold injection, and the MF_S15.Sim2-Crhr2 cluster expresses

Figure 3. Spatial domain analysis of *Sim1*$^+$ MERFISH clusters

(A) Representative MERFISH sections showing the anatomical distribution of spatial domains enriched for *Sim1*$^+$ PVH neurons from a male mouse (Slide 3), color-coded by domain identity.

(B) Sankey plot depicting the proportion of each MERFISH *Sim1*$^+$ PVH neuron subtype within each spatial domain (20% cutoff).

(C–F) *Sim1*$^+$ MERFISH reference atlas UMAP highlighting clusters belonging to Rostral (C), Rostral-Intermediate (D), Caudal-Intermediate (E), and Caudal (F) PVH neuron spatial groups.

(G–J) Representative coronal sections from a male mouse (Slide 3) illustrating the distribution of *Sim1*$^+$ MERFISH neuron types in each spatial PVH group.

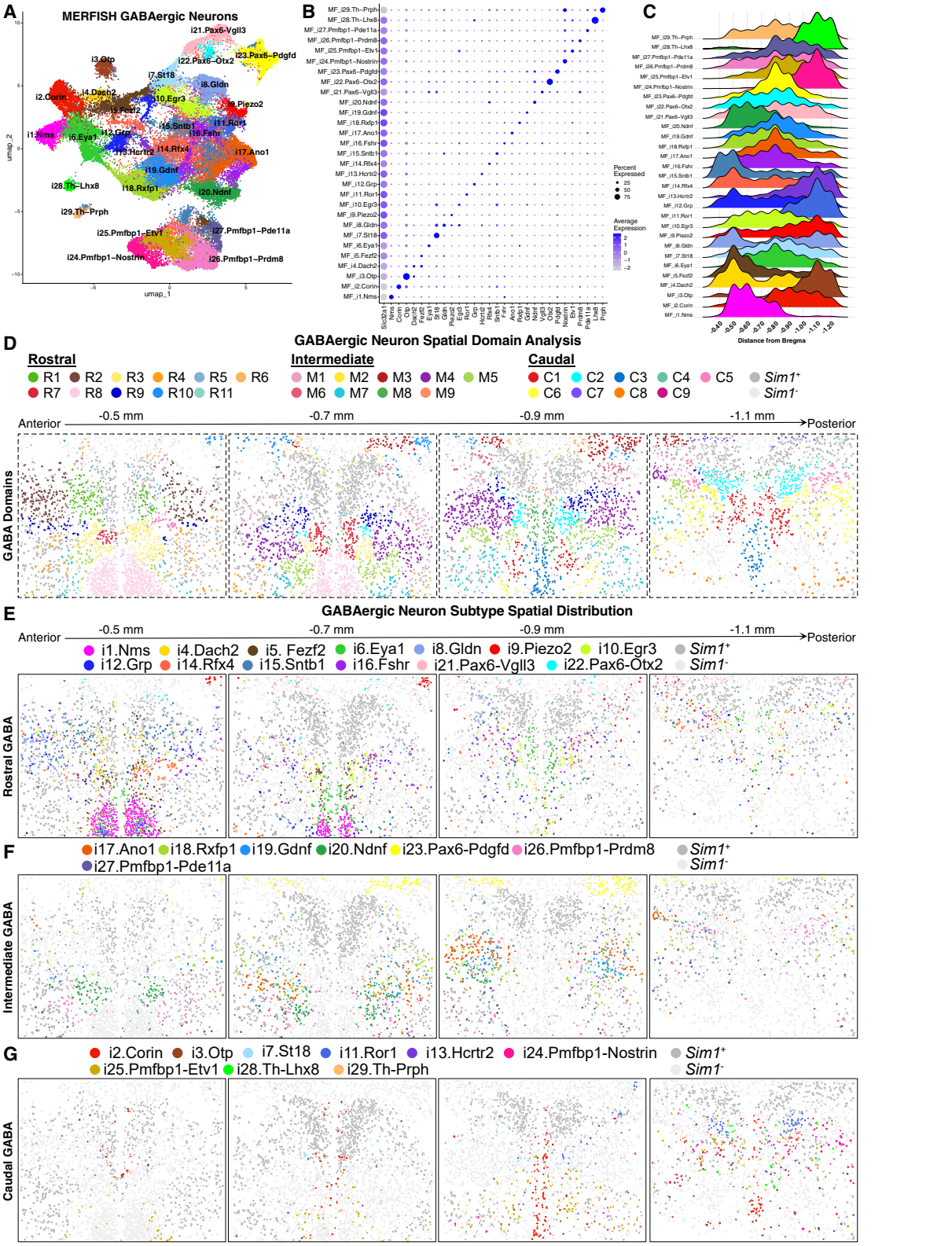

(legend on next page)

both *Trh* and *Adcyap1* (Figures S7D and S7F), suggesting that they are the previously described excitatory afferents to ARC^{Agrp} neurons that drive feeding.[22,52] Indeed, our recent study has revealed that PVH^{Sim2} neurons play an important role in hunger regulation.[53] On the other hand, the MF_S10.Npy2r-Tll2 cluster is marked by neuropeptide Y (NPY) Y2 receptor (*Npy2r*) and tolloid-like protein 2 (*Tll2*; Figures 2C, 3C, and 3G) but does not express other NPY receptors. Given that the orexigenic effects of NPY in the PVH[54] are mediated by NPY1R and NPY5R,[55] we speculate that MF_S10.Npy2r-Tll2 neurons may be modulated by caloric deficit but do not regulate food intake.

The Rostral-Intermediate group consists of four MERFISH clusters that correspond to neuroendocrine populations (Figure 2E): MF_S1.Crh-Scgn, MF_S2.Trh-Satb2, MF_S5.Avp-Pla2r1, and MF_S6.Oxt-Rxfp3 (Figures 3D and 3H). All clusters are primarily located in spatial domain M2, but MF_S6.Oxt-Rxfp3 also has a substantial number of neurons located in spatial domain R5, corresponding to the anterior magnocellular part of the PVH (PVHam; Figures 3A and 3B).[1] Of note, spatial domain analysis did not differentiate parvicellular and magnocellular neuroendocrine subtypes previously defined in rats.[2,7] This may be because spatial domain analysis with SpaDo does not incorporate cytoarchitecture; however, parvicellular and magnocellular cells are also difficult to distinguish with Nissl staining alone in mouse.[1]

The Caudal-Intermediate PVH group comprises MF_S7.Esr2-Inhbb, MF_S8.Esr2-Ret, MF_S9.Npr3-Radx, MF_S13.Pde3a-Tmem215, and MF_S14.Brs3 clusters located primarily in spatial domain M9, which closely corresponds to the ventral zone of the medial parvicellular part of the PVH (PVHmpv; Figures 3A, 3B, 3E, and 3I).[1] Many clusters in this group are marked by genes for hormone and neuropeptide receptors, such as estrogen receptor 2 (*Esr2*) and natriuretic peptide receptor 3 (*Npr3*), which have been reported to regulate stress responses and blood pressure.[56–60] *Esr2* is enriched in two distinct clusters, MF_S7.Esr2-Inhbb and MF_S8.Esr2-Ret (Figures S7G–S7I), while *Npr3* is primarily expressed by MF_S9.Npr3-Radx neurons located in the intermediate and caudal PVH, which exhibit minimal co-labeling with systemically injected Fluoro-Gold (Figures S7J–S7M). Notably, MF_S14.Brs3 is marked by specific expression of bombesin-like receptor subtype 3 (*Brs3*), an important gene for body weight regulation and metabolism (Figures 2C, 3E, and 3I).[61] Consistent with this, PVH^{Brs3} neurons exhibit increased Fos expression following refeeding,[62,63] and chemogenetic manipulation of their activity bidirectionally regulates food intake,[62] similar to PVH^{Mc4r} and PVH^{Pdyn} neurons. Thus, based on prior work, PVH^{Brs3} neurons are of interest for the future study of satiety regulation.

The Caudal PVH group comprises the MF_S11.Aox3, MF_S12.Grp, and MF_S26.Npnt clusters located in spatial domains C4 and C7, which are comparable to the lateral parvicellular (PVHlp) and forniceal (PVHf) parts of the PVH (Figures 3A, 3B, 3F, and 3J). Of interest, the MF_S12.Grp cluster is marked by specific expression of gastrin-releasing peptide (*Grp*; Figures 2C, S3F, and S3J), which is decreased in the PVH following fasting and increased by melanocortin signaling, raising the possibility that these neurons may regulate energy balance.[64]

The remaining *Sim1*$^{+}$ neuronal clusters are primarily located adjacent to the PVH (Figures S8A–S8C). While these peri-PVH clusters express *Sim1*, they are located in separate spatial domains (R2, R4, R9, M1, M6, and C6) and have distinct transcriptional characteristics. With the exception of neurons expressing urocortin 3 (*Ucn3*), which are involved in stress and parenting behaviors,[65,66] neuron subtypes in this region are largely of unknown function and include MF_S16.Ucn3, MF_S17.Onecut3-Frem3, MF_S18.Onecut3-Pvalb, MF_S19.Onecut3-Hmcn1, MF_S20.Gsc-Serpinb1b, MF_S21.Gsc-Nms, MF_S22.Gsc-Nmbr, MF_S23.Ebf2-Hpgd, MF_S24.Ebf2-Hmcn2, and MF_S25.Ebf2-Pou6f2. Consistent with our spatial characterization of these peri-PVH groups (Figures S8A and S8B), previous studies have identified *Onecut3*- and *Gsc*-expressing neurons to be located laterally and ventrally to the PVH.[41,42]

Finally, since previous characterization of PVH neuron populations in human samples has primarily focused on neuroendocrine subtypes,[67–69] we asked whether the PVH neuron populations identified in our mouse transcriptomic study resemble those in humans. To examine this, we performed a comparative analysis between our mouse sc/snRNA-seq atlas and human brain snRNA-seq data. First, we retrieved all cells from dissections containing the PVH from two publicly available human studies[70,71] and clustered them using Seurat 5. Next, as we did for mouse sc/snRNA-seq clustering of PVH neurons, we subset the data to only include *SIM1*$^{+}$ clusters and re-clustered the remaining 3,432 *SIM1*$^{+}$ nuclei, resulting in 21 distinct *SIM1*$^{+}$ neuronal clusters (Figures S8D and S8E; Table S10A). To estimate the transcriptomic similarity between human and mouse PVH neurons, we performed CCA comparing *Sim1*/*SIM1*-positive clusters, which also allowed us to provide the analogous mouse MERFISH cluster identifiers. Strikingly, we observed a high degree of transcriptional correlation across species, with notable similarity between humans and mice for neuroendocrine hormone-, *Sim2*-, and *Ucn3*-expressing neuron populations (Figure S8F; Table S10B).

MERFISH atlas of peri-PVH GABAergic neurons

As noted above, the PVH is surrounded by GABAergic (*Slc32a1*$^{+}$) neurons, some of which project locally into the PVH[38] and are proposed to regulate the HPA axis.[37,72] Specific analysis of GABAergic MERFISH populations included 53,294 neurons

Figure 4. MERFISH spatial transcriptomic profiling of GABAergic neurons surrounding the PVH

(A) UMAP plot showing 53,294 GABAergic neurons.

(B) Dot plot showing the expression of *Slc32a1* and marker genes for GABAergic neuron clusters.

(C) Ridge plot showing the distribution of GABAergic neuronal clusters along the rostral-to-caudal axis.

(D) Representative MERFISH sections showing the anatomical distribution of spatial domains enriched for GABAergic neurons from a male mouse (Slide 3), color-coded by domain identity.

(E–G) Representative coronal MERFISH sections showing the Rostral (E), Intermediate (F), and Caudal (G) spatial distribution of 29 GABAergic neuron types from a male mouse (Slide 3), color-coded by cluster identity.

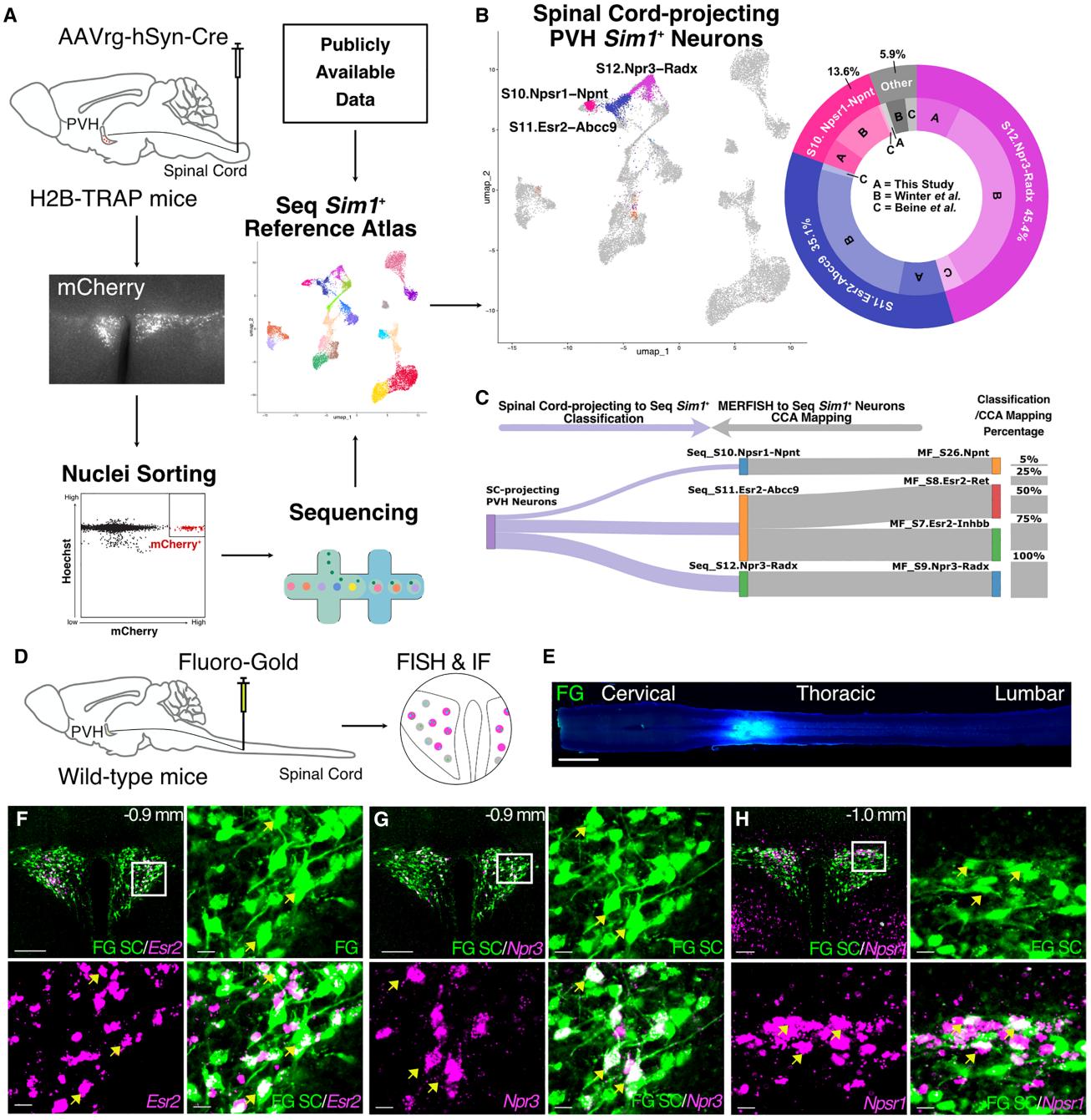

Figure 5. Transcriptomic profiling of spinal cord-projecting PVH *Sim1*$^+$ neurons

(A) Experimental workflow for targeted single-nucleus RNA sequencing of spinal cord-projecting PVH neurons.

(B) Spinal cord-projecting PVH neurons from this study and previously published data[84,85] were classified via the *Sim1*$^+$ sc/snRNA-seq reference atlas and projected into its UMAP space. The donut plot illustrates the proportion of spinal cord-projecting PVH neurons that map to individual sc/snRNA-seq *Sim1*$^+$ neuron clusters annotated by study.

(C) Three-level Sankey plot showing the mapping percentage of spinal cord-projecting PVH neurons classified using the mouse *Sim1*$^+$ sc/snRNA-seq reference atlas (left mapping to center; 5% cutoff) with corresponding *Sim1*$^+$ MERFISH clusters identified via canonical correlation analysis (CCA; right mapping to center). The line thickness represents strength of mapping.

(D) Schematic diagram of retrograde Fluoro-Gold (FG) injection into the thoracic spinal cord. Coronal brain sections containing the PVH were collected for immunofluorescence (IF) and fluorescence *in situ* hybridization (FISH).

(E) Representative longitudinal section of the spinal cord showing the bilateral thoracic injection sites labeled by FG IF. Scale bar, 2 mm.

(legend continued on next page)

that clustered into 29 distinct populations. We labeled each cluster according to the expression of one or more marker genes identified through differential gene expression analysis (Figures 4A and 4B; Table S11A). Next, we performed CCA between MERFISH and sc/snRNA-seq GABAergic neuron clusters to assess transcriptomic agreement between technologies, and this analysis demonstrated a high degree of similarity (Figure S9A; Table S11B). Finally, we plotted the spatial distribution of the GABAergic MERFISH clusters along the rostral-to-caudal axis, grouping clusters according to spatial domains into "Rostral," "Intermediate," or "Caudal" categories (Figures 4C–4G; Figure S9B).

Rostral GABAergic neurons include MF_i1.Nms, MF_i4.Dach2, MF_i5.Fezf2, MF_i6.Eya1, MF_i8.Gldn, MF_i9.Piezo2, MF_i10.Egr3, MF_i12.Grp, MF_i14.Rfx4, MF_i15.Sntb1, MF_i16.Fshr, MF_i21.Pax6-Vgll3, and MF_i22.Pax6-Otx2 (Figures 4D and 4E). Of these, MF_i1.Nms and MF_i12.Grp represent neurons located in the suprachiasmatic nucleus (SCN; Figure 4E). Rostral GABAergic neurons also identify subparaventricular zone (SPZ) neuron populations that have been difficult to target previously. Of interest, the SPZ is the major output of the SCN,[73] and SPZ clusters include MF_i5.Fezf2, MF_i6.Eya1, and MF_i14.Rfx4. Intermediate GABAergic clusters include MF_i17.Ano1, MF_i18.Rxfp1, MF_i19.Gdnf, MF_i20.Ndnf, MF_i26.Pmfbp1-Prdm8, and MF_i27.Pmfbp1-Pde11a neurons residing ventral and lateral to the PVH in the anterior hypothalamic area (AHA), and the MF_i23.Pax6-Pdgfd cluster located dorsal to the PVH (Figure 4F). Finally, the Caudal GABAergic neuron subtypes include MF_i2.Corin and MF_i29.Th-Prph located in the periventricular hypothalamus, the latter of which expresses *Th*, *Ddc*, *Slc18a2*, and *Slc6a3*, suggesting they release dopamine in addition to GABA (Figure 4G). Remaining Caudal clusters include MF_i3.Otp, MF_i7.St18, MF_i11.Ror1, MF_i13.Hcrtr2, MF_i24.Pmfbp1_Nostrin, MF_i25.Pmfbp1-Etv1, and MF_i28.Th-Lhx8 located in the posterior AHA (Figure 4G). Together, this MERFISH analysis offers a valuable molecular characterization of peri-PVH GABAergic neurons.

Targeted transcriptomic profiling of spinal cord-projecting PVH neurons

Numerous studies have demonstrated that PVH neurons project to the spinal cord,[2,4,5,8,9,19,74–79] many of which are thought to activate sympathetic preganglionic neurons in the intermediolateral cell column to regulate cardiometabolic physiology.[19,23,24,75,80–83] Spinal cord-projecting PVH neurons have been sequenced previously[84,85]; however, prior studies did not profile PVH neurons that project to the thoracic spinal cord, where most sympathetic preganglionic neurons are located, and they did not provide molecular markers that differentiate spinal cord-projecting neurons from other PVH neuron subtypes. Therefore, we profiled PVH neurons that project to the thoracic spinal cord and mapped them onto our *Sim1*$^+$ sc/snRNA-seq reference atlas. H2B-TRAP mice[86] were injected with retrograde AAV-Cre into the thoracic (~T2–T4) spinal cord to selectively label the nuclei of spinal cord-projecting PVH neurons with mCherry for subsequent fluorescence-activated nuclei sorting (FANS; Figure 5A). After sequencing and clustering, we merged the thoracic spinal cord-projecting *Sim1*$^+$ neuron data with *Sim1*$^+$ neurons present in previously published spinal cord-projecting datasets.[84,85] Subsequently, we classified the spinal cord-projecting cells based on our *Sim1*$^+$ sc/snRNA-seq reference atlas and projected them onto the reference UMAP. Results showed agreement across all studies, suggesting that spinal cord-projecting PVH neurons share transcriptional similarities regardless of the spinal level to which they project, with most clustering within one of three populations: Seq_S10.Npsr1-Npnt (13.6%), Seq_S11.Esr2-Abcc9 (35.1%), or Seq_S12.Npr3-Radx (45.4%; Figures 5B; Table S12A). Based on *Sim1*$^+$ MERFISH to sc/snRNA-seq CCA mapping, the corresponding MERFISH clusters for spinal cord-projecting populations are MF_S7.Esr2-Inhbb, MF_S8.Esr2-Ret, MF_S9.Npr3-Radx, and MF_S26.Npnt (Figure 5C).

To confirm the molecular identity of spinal cord-projecting PVH neurons, we injected the retrograde tracer Fluoro-Gold into the thoracic spinal cord and subsequently performed FISH for *Esr2*, *Npr3*, or neuropeptide S receptor 1 (*Npsr1)* (Figures 5D and 5E). Our histological analysis revealed colocalization of Fluoro-Gold with the mRNA of all three marker genes we assayed. Notably, the colocalization of *Esr2* and *Npr3* with Fluoro-Gold was predominantly observed in the intermediate and caudal regions of the PVH (Figures 5F and 5G), which is consistent with the spatial patterning of these genes identified by MERFISH (Figure S7I and S7L). Likewise, a separate population of Fluoro-Gold-labeled neurons in the caudal PVH was also found to be positive for *Npsr1* mRNA (Figure 5H), matching the pattern identified by MERFISH (Figure 3J). Together, these data support that there are three predominant and transcriptionally distinct spinal cord-projecting PVH neuron populations that are likely involved in sympathetic regulation. However, the functional role of each specific spinal cord-projecting PVH population is not known and is an important area of future study.

Detection of satiety marker genes in *Sim1*$^+$ neurons with MERFISH

PVH regulation of feeding behavior has been studied extensively, yet the precise PVH neurons mediating satiety are still unknown. Further, several marker genes expressed by PVH neurons have been proposed to be involved in satiety regulation, but the relationship among these genes is unresolved. Therefore, we examined our *Sim1*$^+$ MERFISH atlas to assess the expression patterns of genes associated with satiety. To begin, we analyzed the expression of *Mc4r* as MC4R signaling in the PVH is necessary and sufficient for satiety and body weight regulation.[12–15,21] *Mc4r* is expressed by several *Sim1*$^+$ neuron populations and highly correlated with the expression of *Npy1r*, as expected given its role in feeding behavior (Figures 6A–6C).[87–89] Expression of *Mc4r* and *Npy1r* is widespread throughout the PVH, with an enrichment in the caudal-intermediate region between

(F–H) IF for spinal cord-injected FG and FISH for *Esr2* (F), *Npr3* (G), and *Npsr1* (H) at representative bregma levels. For each, the top-left panel shows a low-magnification view of FG and FISH labeling. Remaining panels provide magnified views of the boxed region for FG IF (top-right), FISH (bottom-left), or both (bottom-right). Yellow arrows indicate representative co-labeled neurons. Low-magnification scale bar, 100 μm, high-magnification scale bar, 20 μm.

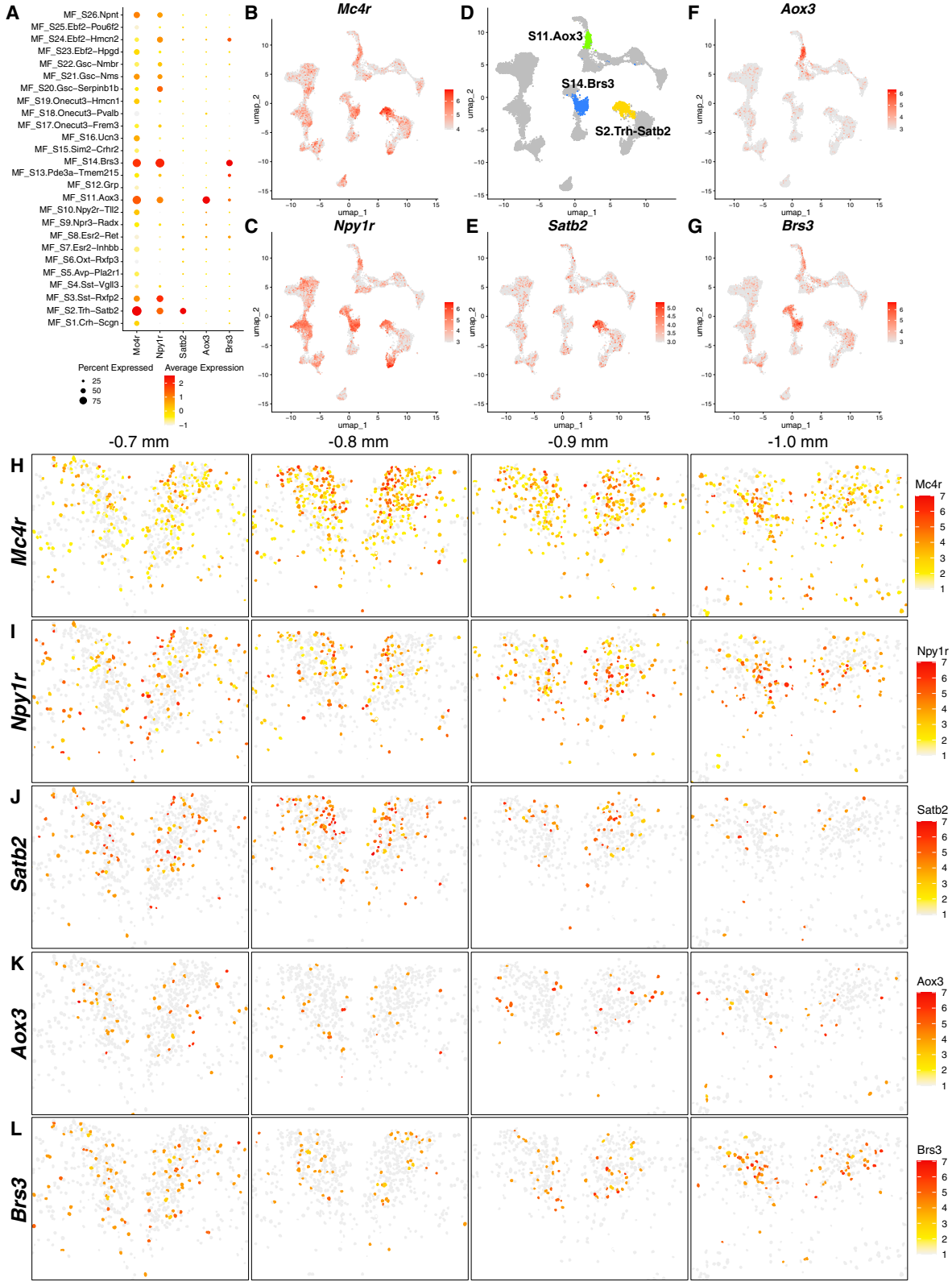

(legend on next page)

bregma levels −0.7 and −1.0 mm (Figures 6H and 6I). Despite *Mc4r* being expressed by multiple PVH neuron subtypes, three clusters display the strongest enrichment: MF_S2.Trh-Satb2, MF_S11.Aox3, and MF_S14.Brs3 (Figures 6A, 6D–6G). These marker genes, *Satb2*, *Aox3*, and *Brs3*, have limited spatial distributions, often enriched within areas of high *Mc4r* and *Npy1r* expression (Figures 6J–6L). MF_S2.Trh-Satb2 neurons have the highest expression of *Mc4r* and represent PVH^{Trh} neurons that project to the median eminence (Figures 1C, 1D, and 1F) to control the hypothalamic-pituitary-thyroid axis, which is consistent with MC4R and NPY regulation of thyroid hormone release during fasting.[90,91] The next highest *Mc4r*-expressing clusters are MF_S11.Aox3 and MF_S14.Brs3, both of which project centrally as they are not labeled by systemic Fluoro-Gold injection (Figures S10A and S10B). MF_S11.Aox3 represents a population of centrally projecting PVH neurons with unknown function(s), while PVH^{Brs3} neurons regulate feeding behavior, as noted above.[62] In support of an interaction between *Brs3* and *Mc4r*, conditional knockout of *Brs3* from *Mc4r*-expressing neurons produces obesity.[92]

Other genes used to investigate PVH satiety-regulating populations, including *Calcr*,[16] *Glp1r*,[15] *Irs4*,[17] *Ntrk2*,[18] *Nos1*,[19] *and Pdyn*,[21] are expressed widely across different PVH neuron subtypes (Figure S10C). Among them, *Calcr* and *Glp1r* have the most restricted expression patterns but are expressed by neuroendocrine and centrally projecting populations. With regard to identifying candidate PVH satiety neurons within our atlas, three clusters express the majority of the satiety genes above, MF_S8.Esr2-Ret, MF_S13.Pde3a-Tmem215, and MF_S14.Brs3 (Figure S10C). As noted before, MF_S14.Brs3 neurons are enriched for *Mc4r* expression and may represent *Mc4r*-expressing satiety neurons. MF_S8.Esr2-Ret and MF_S13.Pde3a-Tmem215 neurons, on the other hand, express little *Mc4r* but co-express *Glp1r* and *Pdyn* (Figures S10C–S10G). Given that PVH^{Pdyn} and PVH^{Glp1r} neurons are key regulators of satiety and body weight,[15,21,93] and PVH^{Mc4r} and PVH^{Pdyn} neurons are distinct satiety-regulating populations,[21] MF_S8.Esr2-Ret and MF_S13.Pde3a-Tmem215 neurons are candidates to be the *Pdyn*-expressing PVH satiety neurons.

Targeted transcriptomic profiling of PVH *Sim1*$^+$ neurons that project to the PB

PVH neurons promote satiety through direct excitatory projections to the PB. PVH^{Mc4r} neurons elicit robust glutamatergic synaptic responses in downstream neurons located in the lateral parabrachial nucleus (LPBN),[12] whereas PVH^{Pdyn} neurons preferentially do so in neurons found in the nearby pre-locus coeruleus (pLC),[21,94] despite each satiety population projecting to both regions. That said, *Mc4r* and *Pdyn* are expressed by multiple PVH neuron subtypes, as noted above, and specific molecular markers for PB-projecting PVH neurons have not been identified. Hence, the precise PVH neurons that regulate satiety are unknown. To elucidate the specific PVH populations that project to the PB, we performed targeted snRNA-seq similar to spinal cord-projecting neuron profiling above. Retrograde Cre virus was injected bilaterally into the PB, targeting the LPBN and adjacent pLC, to selectively label the nuclei of PB-projecting PVH neurons with mCherry. Next, PB-projecting nuclei were isolated, collected via FANS, and sequenced (Figure 7A). After clustering, PB-projecting *Sim1*$^+$ neurons were classified based on our *Sim1*$^+$ PVH sc/snRNA-seq atlas and projected onto the reference UMAP (Figure 7B; Table S12B). Our results show that most of the PB-projecting PVH neurons cluster with one of the following populations: Seq_S11.Esr2-Abcc9 (32.4%), Seq_S12.Npr3-Radx (21.2%), Seq_S15.Brs3 (14.7%), Seq_S16.Pde3a-Tmem215 (7.9%), or Seq_S17.Sfta3-ps (16.9%). Of interest, *Mc4r*- and *Npy1r*-enriched MF_S14.Brs3 neurons correspond to the Seq_S7.Brs3 cluster based on our *Sim1*$^+$ MERFISH to sc/snRNA-seq CCA mapping (Figure 7C). To confirm that PVH^{Brs3} neurons express *Mc4r* and project to the PB, we injected the retrograde tracer cholera toxin subunit B (CTB) into the PB and Cre-dependent AAV-EGFP-L10a into the PVH of *Mc4r*-2A-Cre mice.[12,95] Subsequently, we performed FISH to detect *Brs3* expression in the PVH. Histological analysis revealed triple-labeling of fluorescent signals from *Brs3* FISH, *Mc4r*-positive neurons labeled with EGFP, and PB-projecting PVH neurons labeled with CTB (Figures 7D and 7E). Collectively, these findings support the hypothesis that PVH^{Brs3} neurons regulate satiety.

PVH^{Brs3} neurons regulate feeding via projections to the PB

Given that PVH^{Mc4r} neurons are essential for energy balance and prior studies demonstrated that PVH^{Brs3} neuron inhibition increases food intake,[62] we next asked whether PVH^{Brs3} neurons are important for body weight regulation. To test this, we silenced PVH^{Brs3} neurons by bilaterally injecting an AAV driving Cre-dependent expression of tetanus toxin light chain (TeTxLC) or GFP as control into the PVH of *Brs3*-IRES-Cre mice.[96] Additionally, we injected a cohort of wild-type mice with Cre-dependent AAV-TeTxLC as another control group. Body weights were measured weekly, and after 6 weeks, *Brs3*-IRES-Cre mice receiving TeTxLC gained significantly more body weight compared to both control groups (Figure 7F). This finding demonstrates that PVH^{Brs3} neurons regulate body weight by preventing weight gain.

PVH^{Mc4r} neurons are directly inhibited by ARC^{Agrp} neurons to induce hunger.[12,21] Since PVH^{Brs3} neurons express *Mc4r*, project to the PB, and have been implicated in feeding behavior regulation, we next tested whether they receive synaptic input from ARC^{Agrp}

Figure 6. MERFISH characterization of *Mc4r* and *Npy1r* expression in PVH *Sim1*$^+$ neurons

(A) Dot plot showing marker genes for *Sim1*$^+$ neuron clusters with enriched expression of *Mc4r* and *Npy1r*.

(B and C) Feature plots showing the expression of *Mc4r* (B) and *Npy1r* (C).

(D) *Sim1*$^+$ MERFISH reference atlas UMAP highlighting the S2.Trh-Satb2, S14.Brs3, and S11.Aox3 clusters.

(E–G) Feature plots showing the expression of *Satb2* (E), *Aox3* (F), and *Brs3* (G).

(H–L) Image feature plots showing the spatial expression of *Mc4r* (H), *Npy1r* (I), *Satb2* (J), *Aox3* (K), and *Brs3* (L) from intermediate to caudal PVH at representative bregma levels (−0.7 to −1.0 mm).

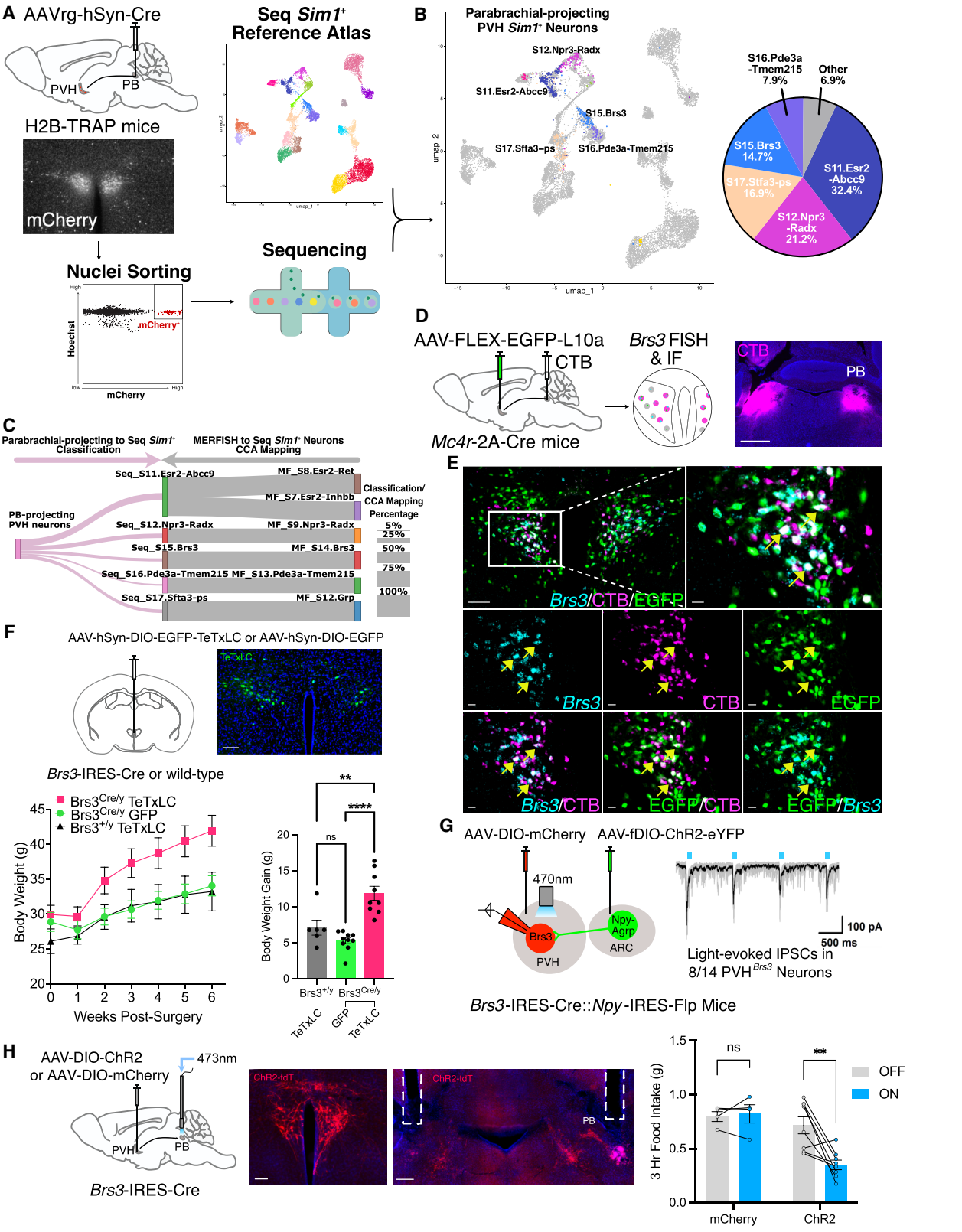

(legend on next page)

neurons.[12,21] ARC^{Agrp} → PVH^{Brs3} neuron connectivity was assessed by channelrhodopsin-2 (ChR2)-assisted circuit mapping (CRACM) using *Brs3*-IRES-Cre::*Npy*-IRES-Flp[97] mice as *Npy* and *Agrp* are co-expressed in the ARC.[98] Cre-dependent AAV-mCherry was injected into the PVH to visualize *Brs3*-expressing neurons for *ex vivo* brain slice electrophysiology recordings, and Flp-dependent AAV-ChR2-eYFP was injected into the ARC to drive ChR2 expression in NPY/AgRP neurons. Light-evoked inhibitory postsynaptic currents (IPSCs) were detected in 8 out of 14 PVH^{Brs3} neuron recordings (Figure 7G), indicating ARC^{Agrp} neurons are monosynaptically connected to many PVH^{Brs3} neurons, further supporting their role in satiety regulation. We next asked if PVH^{Brs3} projections to the PB are sufficient to reduce food intake using *in vivo* optogenetics. *Brs3*-IRES-Cre mice were injected with either Cre-dependent AAV-ChR2 or AAV-mCherry into the PVH, and optical fibers were implanted bilaterally above the PB. Photostimulation of ChR2-expressing PVH^{Brs3} → PB terminals at the onset of the dark cycle significantly reduced food intake (Figure 7H), which is consistent with the effects observed after chemogenetic activation of the entire PVH^{Brs3} population[62] and photostimulation of PVH^{Mc4r} neuron projections to the PB.[12] No reduction in food intake was observed in the mCherry control group after photostimulation. Together, these data establish PVH^{Brs3} neurons as a precise neuronal subtype mediating satiety via projections to the PB.

DISCUSSION

We leveraged single-cell and spatial transcriptomics technologies to develop a high-resolution, spatially resolved atlas of the mouse PVH region. In addition, we conducted targeted snRNA-seq of spinal cord- and PB-projecting PVH neurons to elucidate the neuronal populations involved in regulating sympathetic nervous system activity and feeding behavior, respectively. Prior studies have identified several marker genes for spinal cord-projecting PVH neurons, including *Avp*, *Oxt*,[4,8,99–101] *Bdnf*,[23] *Mc4r*[12], *Nos1*, *Sim1*,[19] *Erbb4*, *Otp*, *Pcsk5*, *Prlr*, and *Zeb2*,[84] but none of these genes are unique to a single PVH neuron type. Given our interest in the regulation of the sympathetic nervous system, we sequenced PVH neurons that project to the thoracic cord, where preganglionic neurons are primarily located. Our results for thoracic-projecting neurons aligned well with publicly available data as all spinal cord-projecting PVH neurons predominantly mapped to Seq_S11.Esr2-Abcc9, Seq_S12.Npr3-Radx, and Seq_S10.Npsr1-Npnt clusters of our *Sim1*$^+$ sc/snRNA-seq reference atlas. The functional roles of these neuron populations remain unknown, but pharmacological manipulation of ESR2 and NPR3 activity in the PVH has been shown to reduce blood pressure.[57,58,60] Of interest, it has long been recognized that a small number of PVH^{Avp} and PVH^{Oxt} neurons project to the spinal cord; however, none of the sequenced spinal cord-projecting PVH neurons mapped to neuroendocrine Seq_S5.Oxt-Rxfp3 or Seq_S6.Avp-Pla2r1 clusters. This is consistent with neuroanatomical tracing studies showing pituitary-projecting PVH neurons do not collateralize to the brainstem and spinal cord.[1,5] Therefore, spinal cord-projecting PVH^{Avp} and PVH^{Oxt} neurons likely belong to the centrally projecting Seq_S11.Esr2-Abcc9 population, which is positive for both *Avp* and *Oxt*.

We sequenced PB-projecting PVH neurons to ascertain their cell type identities because PVH^{Mc4r} and PVH^{Pdyn} satiety neurons represent distinct PB-projecting populations, and multiple neuron subtypes express *Mc4r* and *Pdyn*.[12,21] The majority of *Sim1*$^+$ PB-projecting neurons mapped to five clusters, including two spinal cord-projecting sc/snRNA-seq clusters, Seq_S11.Esr2-Abcc9 and Seq_S12.Npr3-Radx. This may represent similarities in transcriptomes between PB- and spinal cord-projecting PVH neurons or that some PVH neurons collateralize

Figure 7. PVH^{Brs3} neurons project to the parabrachial region and promote satiety

(A) Experimental workflow for targeted single-nucleus RNA sequencing of parabrachial (PB)-projecting PVH neurons.

(B) PB-projecting PVH neurons were classified with the *Sim1*$^+$ sc/snRNA-seq reference atlas and projected into its UMAP space. The pie chart illustrates the proportion of PB-projecting PVH neurons that map to individual *Sim1*$^+$ neuron clusters.

(C) Three-level Sankey plot showing the mapping percentage of PB-projecting PVH neurons classified using the mouse *Sim1*$^+$ sc/snRNA-seq reference atlas (left mapping to center; 5% cutoff) with corresponding *Sim1*$^+$ MERFISH clusters identified via canonical correlation analysis (CCA; right mapping to center). Line thickness represents strength of mapping.

(D) Schematic diagram of retrograde cholera toxin subunit B (CTB) injection into the PB and Cre-dependent AAV-EGFP-L10a injection into the PVH of a *Mc4r*-2A-Cre mouse (left). Representative coronal brain section showing the bilateral PBN CTB injection sites labeled by CTB IF. Scale bar, 250 μm (right).

(E) Top panels show low-magnification (left) and high-magnification (right) views of EGFP IF, CTB IF, and *Brs3* FISH labeling at ∼−0.9 mm. Middle panels display *Brs3* FISH, CTB IF, and EGFP IF, respectively, from left to right. Bottom panels display the overlay of *Brs3* FISH with CTB IF (left), EGFP IF with CTB IF (center), and EGFP IF and *Brs3* FISH (right). Yellow arrows indicate representative triple-labeled neurons. Low-magnification scale bar, 100 μm, high-magnification scale bar = 20 μm.

(F) Schematic of Cre-dependent AAV-tetanus toxin light chain (TeTxLC) or AAV-EGFP injection into the PVH of *Brs3*-IRES-Cre or wild-type mice (top left). Representative PVH injection site labeled with Cre-dependent AAV-EGFP-TeTxLC at ∼−1.0 mm from bregma. Scale bar, 250 μm (top right). Experimental groups include wild-type (Cre-negative) mice injected with Cre-dependent AAV-TeTxLC (n = 6), *Brs3*-IRES-Cre mice injected with Cre-dependent AAV-GFP (n = 10), and *Brs3*-IRES-Cre mice injected with Cre-dependent TeTxLC (n = 9). Body weights were monitored from the day of surgery (week 0) (lower left), and total body weight gained over 6 weeks post-surgery is depicted (lower right). Data shown as mean ± SEM. Statistical analysis was performed using one-way ANOVA followed by Tukey's multiple comparisons test (**p < 0.01, ****p < 0.0001).

(G) Schematic and representative trace from Arc$^{Npy/Agrp}$ → PVH^{Brs3} neuron channelrhodopsin-2 (ChR2)-assisted circuit mapping (CRACM) experiment. Light-evoked IPSCs were detected in 8/14 PVH^{Brs3} neurons.

(H) Schematic showing injection of Cre-dependent ChR2 or mCherry into the PVH and optic fiber implants over the PB in *Brs3*-IRES-Cre mice (left), with representative brain sections showing bilateral ChR2 expression in the PVH at ∼−0.9 mm from bregma (left-center; scale bar, 100 μm), and bilateral fiber tracks in the PB (right-center; scale bar, 250 μm). Food intake (right) was measured over the first 3-h of the dark cycle, with or without photostimulation, in mCherry- (n = 4) and ChR2-expressing mice (n = 8). Data shown as mean ± SEM. Statistical analysis was performed using two-way repeated measures ANOVA followed by Sidak's multiple comparisons test (**p < 0.01).

between these two regions. However, we cannot rule out that retrograde AAV injections were taken up by spinal cord-projecting fibers passing through the PB, which has been observed with some retrograde tracers.[102] PB-projecting neurons did map to three clusters that spinal cord-projecting PVH neurons did not, including Seq_S15.Brs3, Seq_S16.Pde3a-Tmem215, and Seq_S17.Sfta3-ps. Next, we took advantage of the enhanced gene detection capability of MERFISH and compared PVH clusters with the highest expression of *Mc4r* with those identified as PB-projecting. Notably, the MF_S14.Brs3 cluster is among the highest expressors of *Mc4r* and corresponds to the PB-projecting cluster Seq_S15.Brs3. This information, in conjunction with prior work demonstrating that chemogenetic activation of PVH^{Brs3} neurons reduces food intake and inhibition does the opposite,[62] inspired us to further examine their role in energy balance. We show that (1) chronic PVH^{Brs3} neuron silencing causes significant weight gain, (2) they receive direct GABAergic input from hunger-driving ARC^{Agrp} neurons, and (3) stimulation of PVH^{Brs3} neuron projections to the PB reduces food intake. These results are all consistent with PVH^{Brs3} neurons representing *Mc4r*$^{+}$ satiety neurons, yet the effects on food intake that we and others observed were smaller compared to manipulating all PVH^{Mc4r} neurons.[12,62] Thus, there may be multiple PVH^{Mc4r} neuron populations that control food intake. With regard to pinpointing the specific cluster containing PVH^{Pdyn} satiety neurons,[21] MF_S8.Esr2-Ret and MF_S13.Pde3a-Tmem215 neurons correspond to PB-projecting PVH neurons that express *Pdyn* and *Glp1r* but lack *Mc4r*. However, additional studies are required to test whether PB-projecting MF_S8.Esr2-Ret and/or MF_S13.Pde3a-Tmem215 neurons control satiety.

This atlas of the PVH serves as a versatile resource to support future studies of PVH organization and function. It also has several advantages over prior work,[25,26] including a vastly increased sample size, both unbiased and circuit-based molecular profiling, and the ability to resolve spatial information with MERFISH using a gene panel curated for the PVH and surrounding regions. To facilitate accessibility for the scientific community, we uploaded our analyzed sc/snRNA-seq and MERFISH data to the Broad Single Cell Portal (https://singlecell.broadinstitute.org/single_cell/study/SCP2858), an open-access, web-based tool for exploring single-cell genomics data, thus providing a valuable resource for the field of homeostasis.

Limitations of the study

Although our study is the most comprehensive single-cell transcriptomic analysis of the PVH to date, we acknowledge multiple limitations of the current study that provide opportunities for future investigation. First, Nissl staining is not compatible with our MERFISH tissue preparation, so we are unable to directly link transcriptomic information from MERFISH cell types with cytoarchitecture. Second, PVH neurons innervate a wide variety of targets, but our study only provides projection-specific molecular markers for PVH neuron subtypes that project to the pituitary, PB, and spinal cord. Another major limitation of our projection-specific snRNA-seq experiments is the inability to ascertain whether neurons send axon collaterals to additional sites. Of note, some spinal cord-projecting PVH neurons collateralize to the dorsal vagal complex and rostral ventrolateral medulla,[2,77] and some neuroendocrine PVH neurons also collateralize.[103–106] For instance, axon collaterals in the lateral hypothalamus from neuroendocrine PVH^{Crh} neurons are hypothesized to drive stereotypical grooming behavior during acute stress.[106] Thus, PVH neuron subtypes identified as spinal cord- or PB-projecting may project to other sites. Finally, we provide several markers for PVH neurons that project to the PB and spinal cord and discuss them in the context of satiety and sympathetic nervous system regulation; however, we only perform functional studies on PVH^{Brs3} neurons.

RESOURCE AVAILABILITY

Lead contact

Further information and requests for resources and reagents should be directed to and will be fulfilled by the lead contact, Jon Resch (jon-resch@uiowa.edu).

Materials availability

This study did not generate any new and unique reagents.

Data and code availability

Mouse sc/snRNA-seq data from this study have been deposited into the NCBI Gene Expression Omnibus GEO: GSE303256. Allen Brain Cell Atlas mouse sc/snRNA-seq data were downloaded from the following locations: https://allen-brain-cell-atlas.s3.us-west-2.amazonaws.com/index.html#expression_matrices/WMB-10Xv2/20230630/ (10Xv2), and https://allen-brain-cell-atlas.s3.us-west-2.amazonaws.com/index.html#expression_matrices/WMB-10Xv3/20230630/ (10Xv3). Spinal cord-projecting snRNA-seq data not generated in this study were obtained by accessing the publicly available datasets GEO: GSE247594[84] and GSE212409.[85] Human snRNA-seq data were obtained by downloading publicly available datasets, including the Siletti et al.[70] dataset from the Human Brain Cell Atlas Repository (https://datasets.cellxgene.cziscience.com/5e399d37-23d3-4673-8761-9f443c1fdc14.rds) and the Tadross et al.[71] dataset from the University of Cambridge Apollo Repository (https://www.repository.cam.ac.uk/items/cad1c61a-e4e5-4443-ad11-92e4f48b3861). Mouse MERFISH data from this study have been deposited in the Iowa Research Online, IRO:https://iro.uiowa.edu/esploro/outputs/dataset/A-spatial-and-projection-based-transcriptomic-atlas/9984403060302771?institution=01IOWA_INST. All original code and Seurat objects have been deposited to Zenodo: https://doi.org/10.5281/zenodo.15983704. Finally, any additional information required to reanalyze the data reported in this paper is available from the lead contact upon request.

ACKNOWLEDGMENTS

We would like to thank Drs. Mark Andermann, Joel Geerling, and Clifford Saper, as well as the Lowell, Tsai, and Resch laboratories for helpful discussions; Alysia Berns, Jia Yu, and Yanfang Li for technical support; the BNORC Functional Genomics and Bioinformatics Core (P30DK046200) and the Iowa Institute for Human Genetics Genomics Division (IIHG, RRID: SCR_023422) for helpful discussions and technical assistance with sc/snRNA-seq; Zachary Niziolek and the Bauer Core Facility at Harvard University, the BIDMC Flow Cytometry Core, and Heath Vignes, Michael Shey, and Thomas Kaufman of the Flow Cytometry Facility at the University of Iowa Carver College of Medicine for helpful discussions and technical support; the ICCB-Longwood Screening Facility of Harvard Medical School for assistance with the snRNA-seq experiments; Dr. Sayak Mitter and Vizgen support for technical assistance with the MERSCOPE platform; and Mara Jendro and Li-Chun (Queena) Lin for their assistance with MERSCOPE experiments within the Iowa NeuroBank Core in the Iowa Neuroscience Institute at the University of Iowa Carver College of Medicine. This research was funded by the following NIH grants to L.T.T.: R01DK128406; to B.B.L.: R01DK075632, R01DK134427, and R01DK096010; to J.M.R.: R00HL144923 and R01NS141072; and to

M.C.M.: F31HL170784; T.C.B. and M.C.M. were supported by a pharmacological sciences predoctoral training grant T32GM144636. Additional funding to J.M.R. came from the American Heart Association (AHA 935362), a University of Iowa Fraternal Order of Eagles Diabetes Research Center Pilot and Feasibility Catalyst Grant, and an Iowa Neuroscience Institute Early Stage Investigator award from the Carver Trust. Y.L. was supported by a predoctoral fellowship from the American Heart Association (AHA 25PRE1372983). A.M.D. was supported by a postdoctoral fellowship from the Charles A. King Trust.

AUTHOR CONTRIBUTIONS

Conceptualization, Y.L., T.C.B., J.N.C., L.T.T., B.B.L., and J.M.R.; data curation, Y.L., T.C.B., C.L.J., L.T.T., and J.M.R.; formal analysis, T.C.B., S.N., C.L.J., S.J.W., J.N.C., and L.T.T. (sc/snRNA-seq); Y.L., T.C.B., S.N., and J.M.R. (MERFISH); funding acquisition, Y.L., L.T.T., B.B.L., and J.M.R.; investigation, T.C.B., S.N., L.W., D.P., A.W., H.S., J.N.C., and L.T.T. (sc/snRNA-seq); Y.L. and J.M.R. (MERFISH); Y.L., M.C.M., J.T., and E.D.L. (FISH/IF); A.M.D., J.C.M., Z.Y., and J.M.R (electrophysiology and behavioral experiments); methodology, Y.L., T.C.B., S.N., C.L.J., J.N.C., L.T.T., B.B.L., and J.M.R.; project administration, L.T.T., B.B.L., and J.M.R.; resources, L.T.T., B.B.L., and J.M.R.; software, Y.L., T.C.B., S.N., C.L.J., L.T.T., and J.M.R.; supervision, L.T.T., B.B.L., and J.M.R.; validation, T.C.B., S.N., C.L.J., S.J.W., J.N.C., and L.T.T. (sc/snRNA-seq); Y.L., T.C.B., S.N., and J.M.R. (MERFISH); visualization, Y.L., T.C.B., and J.M.R.; writing – original draft, Y.L., T.C.B., L.T.T., B.B.L., and J.M.R. All authors have reviewed and approved the final version of the manuscript.

DECLARATION OF INTERESTS

The authors declare no competing interests.

DECLARATION OF GENERATIVE AI AND AI-ASSISTED TECHNOLOGIES IN THE WRITING PROCESS

During the preparation of this work the author(s) used ChatGPT in order to improve the clarity and readability of the text. After using this tool/service, the author(s) reviewed and edited the content as needed and take(s) full responsibility for the content of the publication.

STAR★METHODS

Detailed methods are provided in the online version of this paper and include the following:

- KEY RESOURCES TABLE
- EXPERIMENTAL MODEL AND STUDY PARTICIPANT DETAILS
  - Mice
- METHOD DETAILS
  - Single-cell/nucleus RNA sequencing tissue collection, library preparation, and sequencing
  - Single-cell/nucleus RNA sequencing quality control
  - Single-cell/nucleus RNA sequencing and data integration
  - Integration of *Sim1*-expressing clusters with publicly available HypoMap and Allen Brain Cell Atlas data
  - Analysis of neuroendocrine neuron transcriptional profiles
  - Single-nucleus RNA sequencing of projection-specific PVH neuron populations
  - Analysis of human PVH single-nucleus RNA sequencing data
  - MERFISH gene panel selection
  - MERFISH tissue collection and sample preparation
  - MERFISH probe hybridization and imaging
  - MERFISH image analysis and cell segmentation
  - MERFISH sequential gene panel preprocessing
  - MERFISH data analysis
  - MERFISH spatial domain analysis
  - Stereotaxic injections and optic fiber implantation
  - AAV and retrograde tracer injections
  - RNAscope fluorescent *in situ* hybridization and immunofluorescence
  - Histological analysis of Cre-reporters and immunofluorescent experiments
  - Body weight measurements after PVH^{Brs3} neuron silencing
  - Channelrhodopsin-2 (ChR2)-assisted circuit mapping (CRACM)
  - Food intake measurements after PVH^{Brs3} neuron → PB optogenetic stimulation
- QUANTIFICATION AND STATISTICAL ANALYSIS
  - Quantification of PVH neuroendocrine neurons
  - Statistical analysis

SUPPLEMENTAL INFORMATION

Supplemental information can be found online at https://doi.org/10.1016/j.celrep.2025.116904.

Received: July 31, 2025
Revised: November 21, 2025
Accepted: December 24, 2025
Published: January 23, 2026

REFERENCES

1. Biag, J., Huang, Y., Gou, L., Hintiryan, H., Askarinam, A., Hahn, J.D., Toga, A.W., and Dong, H.W. (2012). Cyto- and chemoarchitecture of the hypothalamic paraventricular nucleus in the C57BL/6J male mouse: a study of immunostaining and multiple fluorescent tract tracing. J. Comp. Neurol. *520*, 6–33. https://doi.org/10.1002/cne.22698.
2. Swanson, L.W., and Kuypers, H.G. (1980). The paraventricular nucleus of the hypothalamus: cytoarchitectonic subdivisions and organization of projections to the pituitary, dorsal vagal complex, and spinal cord as demonstrated by retrograde fluorescence double-labeling methods. J. Comp. Neurol. *194*, 555–570. https://doi.org/10.1002/cne.901940306.
3. Simmons, D.M., and Swanson, L.W. (2009). Comparison of the spatial distribution of seven types of neuroendocrine neurons in the rat paraventricular nucleus: toward a global 3D model. J. Comp. Neurol. *516*, 423–441. https://doi.org/10.1002/cne.22126.
4. Sawchenko, P.E., and Swanson, L.W. (1982). Immunohistochemical identification of neurons in the paraventricular nucleus of the hypothalamus that project to the medulla or to the spinal cord in the rat. J. Comp. Neurol. *205*, 260–272. https://doi.org/10.1002/cne.902050306.
5. Swanson, L.W., Sawchenko, P.E., Wiegand, S.J., and Price, J.L. (1980). Separate neurons in the paraventricular nucleus project to the median eminence and to the medulla or spinal cord. Brain Res. *198*, 190–195. https://doi.org/10.1016/0006-8993(80)90354-6.
6. Swanson, L.W., and Sawchenko, P.E. (1980). Paraventricular nucleus: a site for the integration of neuroendocrine and autonomic mechanisms. Neuroendocrinology *31*, 410–417. https://doi.org/10.1159/000123111.
7. Armstrong, W.E., Warach, S., Hatton, G.I., and McNeill, T.H. (1980). Subnuclei in the rat hypothalamic paraventricular nucleus: a cytoarchitectural, horseradish peroxidase and immunocytochemical analysis. Neuroscience *5*, 1931–1958. https://doi.org/10.1016/0306-4522(80)90040-8.
8. Swanson, L.W. (1977). Immunohistochemical evidence for a neurophysin-containing autonomic pathway arising in the paraventricular nucleus of the hypothalamus. Brain Res. *128*, 346–353. https://doi.org/10.1016/0006-8993(77)91000-9.
9. Saper, C.B., Loewy, A.D., Swanson, L.W., and Cowan, W.M. (1976). Direct hypothalamo-autonomic connections. Brain Res. *117*, 305–312. https://doi.org/10.1016/0006-8993(76)90738-1.
10. Geerling, J.C., Shin, J.W., Chimenti, P.C., and Loewy, A.D. (2010). Paraventricular hypothalamic nucleus: axonal projections to the brainstem. J. Comp. Neurol. *518*, 1460–1499. https://doi.org/10.1002/cne.22283.

11. Krashes, M.J., Lowell, B.B., and Garfield, A.S. (2016). Melanocortin-4 receptor–regulated energy homeostasis. Nat. Neurosci. *19*, 206–219. https://doi.org/10.1038/nn.4202.

12. Garfield, A.S., Li, C., Madara, J.C., Shah, B.P., Webber, E., Steger, J.S., Campbell, J.N., Gavrilova, O., Lee, C.E., Olson, D.P., et al. (2015). A neural basis for melanocortin-4 receptor-regulated appetite. Nat. Neurosci. *18*, 863–871. https://doi.org/10.1038/nn.4011.

13. Shah, B.P., Vong, L., Olson, D.P., Koda, S., Krashes, M.J., Ye, C., Yang, Z., Fuller, P.M., Elmquist, J.K., and Lowell, B.B. (2014). MC4R-expressing glutamatergic neurons in the paraventricular hypothalamus regulate feeding and are synaptically connected to the parabrachial nucleus. Proc. Natl. Acad. Sci. USA *111*, 13193–13198. https://doi.org/10.1073/pnas.1407843111.

14. Balthasar, N., Dalgaard, L.T., Lee, C.E., Yu, J., Funahashi, H., Williams, T., Ferreira, M., Tang, V., McGovern, R.A., Kenny, C.D., et al. (2005). Divergence of melanocortin pathways in the control of food intake and energy expenditure. Cell *123*, 493–505. https://doi.org/10.1016/j.cell.2005.08.035.

15. Li, C., Navarrete, J., Liang-Guallpa, J., Lu, C., Funderburk, S.C., Chang, R.B., Liberles, S.D., Olson, D.P., and Krashes, M.J. (2019). Defined Paraventricular Hypothalamic Populations Exhibit Differential Responses to Food Contingent on Caloric State. Cell Metab. *29*, 681–694.e5. https://doi.org/10.1016/j.cmet.2018.10.016.

16. Gonzalez, I.E., Ramirez-Matias, J., Lu, C., Pan, W., Zhu, A., Myers, M.G., and Olson, D.P. (2021). Paraventricular Calcitonin Receptor-Expressing Neurons Modulate Energy Homeostasis in Male Mice. Endocrinology *162*, bqab072. https://doi.org/10.1210/endocr/bqab072.

17. Sutton Hickey, A.K., Gonzalez, I.E., Sadagurski, M., Rajala, M., Lu, C., Allison, M.B., Adams, J.M., Myers, M.G., White, M.F., and Olson, D.P. (2020). Paraventricular, subparaventricular and periventricular hypothalamic IRS4-expressing neurons are required for normal energy balance. Sci. Rep. *10*, 5546. https://doi.org/10.1038/s41598-020-62468-z.

18. An, J.J., Kinney, C.E., Tan, J.W., Liao, G.Y., Kremer, E.J., and Xu, B. (2020). TrkB-expressing paraventricular hypothalamic neurons suppress appetite through multiple neurocircuits. Nat. Commun. *11*, 1729. https://doi.org/10.1038/s41467-020-15537-w.

19. Sutton, A.K., Pei, H., Burnett, K.H., Myers, M.G., Jr., Rhodes, C.J., and Olson, D.P. (2014). Control of food intake and energy expenditure by Nos1 neurons of the paraventricular hypothalamus. J. Neurosci. *34*, 15306–15318. https://doi.org/10.1523/JNEUROSCI.0226-14.2014.

20. Pei, H., Sutton, A.K., Burnett, K.H., Fuller, P.M., and Olson, D.P. (2014). AVP neurons in the paraventricular nucleus of the hypothalamus regulate feeding. Mol. Metab. *3*, 209–215. https://doi.org/10.1016/j.molmet.2013.12.006.

21. Li, M.M., Madara, J.C., Steger, J.S., Krashes, M.J., Balthasar, N., Campbell, J.N., Resch, J.M., Conley, N.J., Garfield, A.S., and Lowell, B.B. (2019). The Paraventricular Hypothalamus Regulates Satiety and Prevents Obesity via Two Genetically Distinct Circuits. Neuron *102*, 653–667.e6. https://doi.org/10.1016/j.neuron.2019.02.028.

22. Krashes, M.J., Shah, B.P., Madara, J.C., Olson, D.P., Strochlic, D.E., Garfield, A.S., Vong, L., Pei, H., Watabe-Uchida, M., Uchida, N., et al. (2014). An excitatory paraventricular nucleus to AgRP neuron circuit that drives hunger. Nature *507*, 238–242. https://doi.org/10.1038/nature12956.

23. An, J.J., Liao, G.Y., Kinney, C.E., Sahibzada, N., and Xu, B. (2015). Discrete BDNF Neurons in the Paraventricular Hypothalamus Control Feeding and Energy Expenditure. Cell Metab. *22*, 175–188. https://doi.org/10.1016/j.cmet.2015.05.008.

24. Wang, P., Loh, K.H., Wu, M., Morgan, D.A., Schneeberger, M., Yu, X., Chi, J., Kosse, C., Kim, D., Rahmouni, K., et al. (2020). A leptin–BDNF pathway regulating sympathetic innervation of adipose tissue. Nature *583*, 839–844. https://doi.org/10.1038/s41586-020-2527-y.

25. Berkhout, J.B., Poormoghadam, D., Yi, C., Kalsbeek, A., Meijer, O.C., and Mahfouz, A. (2024). An integrated single-cell RNA-seq atlas of the mouse hypothalamic paraventricular nucleus links transcriptomic and functional types. J. Neuroendocrinol. *36*, e13367. https://doi.org/10.1111/jne.13367.

26. Xu, S., Yang, H., Menon, V., Lemire, A.L., Wang, L., Henry, F.E., Turaga, S.C., and Sternson, S.M. (2020). Behavioral state coding by molecularly defined paraventricular hypothalamic cell type ensembles. Science *370*, eabb2494. https://doi.org/10.1126/science.abb2494.

27. Romanov, R.A., Alpár, A., Zhang, M.D., Zeisel, A., Calas, A., Landry, M., Fuszard, M., Shirran, S.L., Schnell, R., Dobolyi, Á., et al. (2015). A secretagogin locus of the mammalian hypothalamus controls stress hormone release. EMBO J. *34*, 36–54. https://doi.org/10.15252/embj.201488977.

28. Zhang, M., Pan, X., Jung, W., Halpern, A.R., Eichhorn, S.W., Lei, Z., Cohen, L., Smith, K.A., Tasic, B., Yao, Z., et al. (2023). Molecularly defined and spatially resolved cell atlas of the whole mouse brain. Nature *624*, 343–354. https://doi.org/10.1038/s41586-023-06808-9.

29. Yao, Z., van Velthoven, C.T.J., Kunst, M., Zhang, M., McMillen, D., Lee, C., Jung, W., Goldy, J., Abdelhak, A., Aitken, M., et al. (2023). A high-resolution transcriptomic and spatial atlas of cell types in the whole mouse brain. Nature *624*, 317–332. https://doi.org/10.1038/s41586-023-06812-z.

30. Shi, H., He, Y., Zhou, Y., Huang, J., Maher, K., Wang, B., Tang, Z., Luo, S., Tan, P., Wu, M., et al. (2023). Spatial atlas of the mouse central nervous system at molecular resolution. Nature *622*, 552–561. https://doi.org/10.1038/s41586-023-06569-5.

31. Langlieb, J., Sachdev, N.S., Balderrama, K.S., Nadaf, N.M., Raj, M., Murray, E., Webber, J.T., Vanderburg, C., Gazestani, V., Tward, D., et al. (2023). The molecular cytoarchitecture of the adult mouse brain. Nature *624*, 333–342. https://doi.org/10.1038/s41586-023-06818-7.

32. Steuernagel, L., Lam, B.Y.H., Klemm, P., Dowsett, G.K.C., Bauder, C.A., Tadross, J.A., Hitschfeld, T.S., del Rio Martin, A., Chen, W., de Solis, A.J., et al. (2022). HypoMap—a unified single-cell gene expression atlas of the murine hypothalamus. Nat. Metab. *4*, 1402–1419. https://doi.org/10.1038/s42255-022-00657-y.

33. Macosko, E.Z., Basu, A., Satija, R., Nemesh, J., Shekhar, K., Goldman, M., Tirosh, I., Bialas, A.R., Kamitaki, N., Martersteck, E.M., et al. (2015). Highly Parallel Genome-wide Expression Profiling of Individual Cells Using Nanoliter Droplets. Cell *161*, 1202–1214. https://doi.org/10.1016/j.cell.2015.05.002.

34. Habib, N., Avraham-Davidi, I., Basu, A., Burks, T., Shekhar, K., Hofree, M., Choudhury, S.R., Aguet, F., Gelfand, E., Ardlie, K., et al. (2017). Massively parallel single-nucleus RNA-seq with DroNc-seq. Nat. Methods *14*, 955–958. https://doi.org/10.1038/nmeth.4407.

35. Hao, Y., Stuart, T., Kowalski, M.H., Choudhary, S., Hoffman, P., Hartman, A., Srivastava, A., Molla, G., Madad, S., Fernandez-Granda, C., and Satija, R. (2024). Dictionary learning for integrative, multimodal and scalable single-cell analysis. Nat. Biotechnol. *42*, 293–304. https://doi.org/10.1038/s41587-023-01767-y.

36. Stuart, T., Butler, A., Hoffman, P., Hafemeister, C., Papalexi, E., Mauck, W.M., 3rd, Hao, Y., Stoeckius, M., Smibert, P., and Satija, R. (2019). Comprehensive Integration of Single-Cell Data. Cell *177*, 1888–1902.e21. https://doi.org/10.1016/j.cell.2019.05.031.

37. Cullinan, W.E., Ziegler, D.R., and Herman, J.P. (2008). Functional role of local GABAergic influences on the HPA axis. Brain Struct. Funct. *213*, 63–72. https://doi.org/10.1007/s00429-008-0192-2.

38. Roland, B.L., and Sawchenko, P.E. (1993). Local origins of some GABAergic projections to the paraventricular and supraoptic nuclei of the hypothalamus in the rat. J. Comp. Neurol. *332*, 123–143. https://doi.org/10.1002/cne.903320109.

39. Michaud, J.L., Rosenquist, T., May, N.R., and Fan, C.M. (1998). Development of neuroendocrine lineages requires the bHLH-PAS transcription factor SIM1. Genes Dev. *12*, 3264–3275. https://doi.org/10.1101/gad.12.20.3264.

40. Lein, E.S., Hawrylycz, M.J., Ao, N., Ayres, M., Bensinger, A., Bernard, A., Boe, A.F., Boguski, M.S., Brockway, K.S., Byrnes, E.J., et al. (2007). Genome-wide atlas of gene expression in the adult mouse brain. Nature *445*, 168–176. https://doi.org/10.1038/nature05453.

41. Zupancic, M., Tretiakov, E., Mate, Z., Erdelyi, F., Szabo, G., Clotman, F., Hokfelt, T., Harkany, T., and Keimpema, E. (2023). Brain-wide mapping of efferent projections of glutamatergic (Onecut3(+)) neurons in the lateral mouse hypothalamus. Acta Physiol. *238*, e13973. https://doi.org/10.1111/apha.13973.

42. Asbreuk, C.H.J., van Schaick, H.S.A., Cox, J.J., Smidt, M.P., and Burbach, J.P.H. (2002). Survey for paired-like homeodomain gene expression in the hypothalamus: restricted expression patterns of Rx, Alx4 and goosecoid. Neuroscience *114*, 883–889. https://doi.org/10.1016/s0306-4522(02)00325-1.

43. Merchenthaler, I. (1991). Neurons with access to the general circulation in the central nervous system of the rat: a retrograde tracing study with fluoro-gold. Neuroscience *44*, 655–662. https://doi.org/10.1016/0306-4522(91)90085-3.

44. Ambalavanar, R., and Morris, R. (1989). Fluoro-Gold injected either subcutaneously or intravascularly results in extensive retrograde labelling of CNS neurones having axons terminating outside the blood-brain barrier. Brain Res. *505*, 171–175. https://doi.org/10.1016/0006-8993(89)90133-9.

45. Minami, S., Kamegai, J., Sugihara, H., Suzuki, N., and Wakabayashi, I. (1998). Growth hormone inhibits its own secretion by acting on the hypothalamus through its receptors on neuropeptide Y neurons in the arcuate nucleus and somatostatin neurons in the periventricular nucleus. Endocr. J. *45*, S19–S26. https://doi.org/10.1507/endocrj.45.suppl_s19.

46. Nardone, S., De Luca, R., Zito, A., Klymko, N., Nicoloutsopoulos, D., Amsalem, O., Brannigan, C., Resch, J.M., Jacobs, C.L., Pant, D., et al. (2024). A spatially-resolved transcriptional atlas of the murine dorsal pons at single-cell resolution. Nat. Commun. *15*, 1966. https://doi.org/10.1038/s41467-024-45907-7.

47. Chen, K.H., Boettiger, A.N., Moffitt, J.R., Wang, S., and Zhuang, X. (2015). RNA imaging. Spatially resolved, highly multiplexed RNA profiling in single cells. Science *348*, aaa6090. https://doi.org/10.1126/science.aaa6090.

48. Hartman, A., and Satija, R. (2024). Comparative analysis of multiplexed in situ gene expression profiling technologies. eLife *13*, RP96949. https://doi.org/10.7554/elife.96949.1.

49. Paxinos, G., and Franklin, K.B.J. (2019). Paxinos and Franklin's the Mouse Brain in Stereotaxic Coordinates, Fifth edition (Academic Press, an imprint of Elsevier).

50. Pachitariu, M., and Stringer, C. (2022). Cellpose 2.0: how to train your own model. Nat. Methods *19*, 1634–1641. https://doi.org/10.1038/s41592-022-01663-4.

51. Duan, B., Chen, S., Cheng, X., and Liu, Q. (2024). Multi-slice spatial transcriptome domain analysis with SpaDo. Genome Biol. *25*, 73. https://doi.org/10.1186/s13059-024-03213-x.

52. Grzelka, K., Wilhelms, H., Dodt, S., Dreisow, M.L., Madara, J.C., Walker, S.J., Wu, C., Wang, D., Lowell, B.B., and Fenselau, H. (2023). A synaptic amplifier of hunger for regaining body weight in the hypothalamus. Cell Metab. *35*, 770–785.e5. https://doi.org/10.1016/j.cmet.2023.03.002.

53. Walker, S.J., Lowenstein, E.D., Douglass, A.M., Madara, J.C., Resch, J.M., Tao, J., and Lowell, B.B. (2025). A hypothalamic circuit for anticipating future changes in energy balance. Preprint at bioRxiv. https://doi.org/10.1101/2025.09.27.678865.

54. Lowell, B.B. (2019). New Neuroscience of Homeostasis and Drives for Food, Water, and Salt. N. Engl. J. Med. *380*, 459–471. https://doi.org/10.1056/NEJMra1812053.

55. Nguyen, A.D., Mitchell, N.F., Lin, S., Macia, L., Yulyaningsih, E., Baldock, P.A., Enriquez, R.F., Zhang, L., Shi, Y.C., Zolotukhin, S., et al. (2012). Y1 and Y5 receptors are both required for the regulation of food intake and energy homeostasis in mice. PLoS One *7*, e40191. https://doi.org/10.1371/journal.pone.0040191.

56. Isgor, C., Cecchi, M., Kabbaj, M., Akil, H., and Watson, S.J. (2003). Estrogen receptor beta in the paraventricular nucleus of hypothalamus regulates the neuroendocrine response to stress and is regulated by corticosterone. Neuroscience *121*, 837–845. https://doi.org/10.1016/s0306-4522(03)00561-x.

57. Gingerich, S., and Krukoff, T.L. (2006). Estrogen in the paraventricular nucleus attenuates L-glutamate-induced increases in mean arterial pressure through estrogen receptor beta and NO. Hypertension *48*, 1130–1136. https://doi.org/10.1161/01.HYP.0000248754.67128.ff.

58. Milner, T.A., Contoreggi, N.H., Yu, F., Johnson, M.A., Wang, G., Woods, C., Mazid, S., Van Kempen, T.A., Waters, E.M., McEwen, B.S., et al. (2021). Estrogen Receptor beta Contributes to Both Hypertension and Hypothalamic Plasticity in a Mouse Model of Peri-Menopause. J. Neurosci. *41*, 5190–5205. https://doi.org/10.1523/JNEUROSCI.0164-21.2021.

59. Sommer, G., Rodriguez Lopez, C., Hirschkorn, A., Calimano, G., Marques-Lopes, J., Milner, T.A., and Glass, M.J. (2024). Estrogen Receptor Beta Agonist Influences Presynaptic NMDA Receptor Distribution in the Paraventricular Hypothalamic Nucleus Following Hypertension in a Mouse Model of Perimenopause. Biology *13*, 819. https://doi.org/10.3390/biology13100819.

60. Zheng, H., Patel, T.A., Liu, X., and Patel, K.P. (2023). C-type natriuretic peptide (CNP) in the paraventricular nucleus-mediated renal sympathoinhibition. Front. Physiol. *14*, 1162699. https://doi.org/10.3389/fphys.2023.1162699.

61. Xiao, C., and Reitman, M.L. (2016). Bombesin-Like Receptor 3: Physiology of a Functional Orphan. Trends Endocrinol. Metab. *27*, 603–605. https://doi.org/10.1016/j.tem.2016.03.003.

62. Pinol, R.A., Zahler, S.H., Li, C., Saha, A., Tan, B.K., Skop, V., Gavrilova, O., Xiao, C., Krashes, M.J., and Reitman, M.L. (2018). Brs3 neurons in the mouse dorsomedial hypothalamus regulate body temperature, energy expenditure, and heart rate, but not food intake. Nat. Neurosci. *21*, 1530–1540. https://doi.org/10.1038/s41593-018-0249-3.

63. Maruyama, M., Hotta, N., Nio, Y., Hamagami, K., Nagi, T., Funata, M., Sakamoto, J., Nakakariya, M., Amano, N., Nishida, M., et al. (2018). Bombesin receptor subtype-3-expressing neurons regulate energy homeostasis through a novel neuronal pathway in the hypothalamus. Brain Behav. *8*, e00881. https://doi.org/10.1002/brb3.881.

64. Ladenheim, E.E., Behles, R.R., Bi, S., and Moran, T.H. (2009). Gastrin-releasing peptide messenger ribonucleic acid expression in the hypothalamic paraventricular nucleus is altered by melanocortin receptor stimulation and food deprivation. Endocrinology *150*, 672–678. https://doi.org/10.1210/en.2008-0559.

65. Autry, A.E., Wu, Z., Kapoor, V., Kohl, J., Bambah-Mukku, D., Rubinstein, N.D., Marin-Rodriguez, B., Carta, I., Sedwick, V., Tang, M., and Dulac, C. (2021). Urocortin-3 neurons in the mouse perifornical area promote infant-directed neglect and aggression. eLife *10*, e64680. https://doi.org/10.7554/eLife.64680.

66. van-Hover, C., and Li, C. (2015). Stress-activated afferent inputs into the anterior parvicellular part of the paraventricular nucleus of the hypothalamus: Insights into urocortin 3 neuron activation. Brain Res. *1611*, 29–43. https://doi.org/10.1016/j.brainres.2015.03.009.

67. Mihaly, E., Fekete, C., Tatro, J.B., Liposits, Z., Stopa, E.G., and Lechan, R.M. (2000). Hypophysiotropic thyrotropin-releasing hormone-synthesizing neurons in the human hypothalamus are innervated by neuropeptide Y, agouti-related protein, and alpha-melanocyte-stimulating hormone. J. Clin. Endocrinol. Metab. *85*, 2596–2603. https://doi.org/10.1210/jcem.85.7.6662.

68. Gai, W.P., Geffen, L.B., and Blessing, W.W. (1990). Galanin immunoreactive neurons in the human hypothalamus: colocalization with vasopressin-containing neurons. J. Comp. Neurol. *298*, 265–280. https://doi.org/10.1002/cne.902980302.

69. Krolewski, D.M., Medina, A., Kerman, I.A., Bernard, R., Burke, S., Thompson, R.C., Bunney, W.E., Jr., Schatzberg, A.F., Myers, R.M., Akil, H., et al. (2010). Expression patterns of corticotropin-releasing factor, arginine vasopressin, histidine decarboxylase, melanin-concentrating hormone, and orexin genes in the human hypothalamus. J. Comp. Neurol. *518*, 4591–4611. https://doi.org/10.1002/cne.22480.

70. Siletti, K., Hodge, R., Mossi Albiach, A., Lee, K.W., Ding, S.L., Hu, L., Lönnerberg, P., Bakken, T., Casper, T., Clark, M., et al. (2023). Transcriptomic diversity of cell types across the adult human brain. Science *382*, eadd7046. https://doi.org/10.1126/science.add7046.

71. Tadross, J.A., Steuernagel, L., Dowsett, G.K.C., Kentistou, K.A., Lundh, S., Porniece, M., Klemm, P., Rainbow, K., Hvid, H., Kania, K., et al. (2025). A comprehensive spatio-cellular map of the human hypothalamus. Nature *639*, 708–716. https://doi.org/10.1038/s41586-024-08504-8.

72. Herman, J.P., Tasker, J.G., Ziegler, D.R., and Cullinan, W.E. (2002). Local circuit regulation of paraventricular nucleus stress integration: glutamate-GABA connections. Pharmacol. Biochem. Behav. *71*, 457–468. https://doi.org/10.1016/s0091-3057(01)00681-5.

73. Watts, A.G., and Swanson, L.W. (1987). Efferent projections of the suprachiasmatic nucleus: II. Studies using retrograde transport of fluorescent dyes and simultaneous peptide immunohistochemistry in the rat. J. Comp. Neurol. *258*, 230–252. https://doi.org/10.1002/cne.902580205.

74. Stocker, S.D., Cunningham, J.T., and Toney, G.M. (2004). Water deprivation increases Fos immunoreactivity in PVN autonomic neurons with projections to the spinal cord and rostral ventrolateral medulla. Am. J. Physiol. Regul. Integr. Comp. Physiol. *287*, R1172–R1183. https://doi.org/10.1152/ajpregu.00394.2004.

75. Pyner, S., and Coote, J.H. (2000). Identification of branching paraventricular neurons of the hypothalamus that project to the rostroventrolateral medulla and spinal cord. Neuroscience *100*, 549–556. https://doi.org/10.1016/s0306-4522(00)00283-9.

76. Toth, Z.E., Gallatz, K., Fodor, M., and Palkovits, M. (1999). Decussations of the descending paraventricular pathways to the brainstem and spinal cord autonomic centers. J. Comp. Neurol. *414*, 255–266.

77. Shafton, A.D., Ryan, A., and Badoer, E. (1998). Neurons in the hypothalamic paraventricular nucleus send collaterals to the spinal cord and to the rostral ventrolateral medulla in the rat. Brain Res. *801*, 239–243. https://doi.org/10.1016/s0006-8993(98)00587-3.

78. Zheng, J.Q., Seki, M., Hayakawa, T., Ito, H., and Zyo, K. (1995). Descending projections from the paraventricular hypothalamic nucleus to the spinal cord: anterograde tracing study in the rat. Okajimas Folia Anat. Jpn. *72*, 119–135. https://doi.org/10.2535/ofaj1936.72.2-3_119.

79. Luiten, P.G., ter Horst, G.J., Karst, H., and Steffens, A.B. (1985). The course of paraventricular hypothalamic efferents to autonomic structures in medulla and spinal cord. Brain Res. *329*, 374–378. https://doi.org/10.1016/0006-8993(85)90554-2.

80. Zhang, Z., Su, J., Tang, J., Chung, L., Page, J.C., Winter, C.C., Liu, Y., Kegeles, E., Conti, S., Zhang, Y., et al. (2024). Spinal projecting neurons in rostral ventromedial medulla co-regulate motor and sympathetic tone. Cell *187*, 3427–3444.e21. https://doi.org/10.1016/j.cell.2024.04.022.

81. Nunn, N., Womack, M., Dart, C., and Barrett-Jolley, R. (2011). Function and pharmacology of spinally-projecting sympathetic pre-autonomic neurones in the paraventricular nucleus of the hypothalamus. Curr. Neuropharmacol. *9*, 262–277. https://doi.org/10.2174/157015911795596531.

82. Carrasco, M., Portillo, F., Larsen, P.J., and Vallo, J.J. (2001). Insulin and glucose administration stimulates Fos expression in neurones of the paraventricular nucleus that project to autonomic preganglionic structures. J. Neuroendocrinol. *13*, 339–346. https://doi.org/10.1046/j.1365-2826.2001.00631.x.

83. Badoer, E., McKinley, M.J., Oldfield, B.J., and McAllen, R.M. (1993). A comparison of hypotensive and non-hypotensive hemorrhage on Fos expression in spinally projecting neurons of the paraventricular nucleus and rostral ventrolateral medulla. Brain Res. *610*, 216–223. https://doi.org/10.1016/0006-8993(93)91403-f.

84. Winter, C.C., Jacobi, A., Su, J., Chung, L., van Velthoven, C.T.J., Yao, Z., Lee, C., Zhang, Z., Yu, S., Gao, K., et al. (2023). A transcriptomic taxonomy of mouse brain-wide spinal projecting neurons. Nature *624*, 403–414. https://doi.org/10.1038/s41586-023-06817-8.

85. Beine, Z., Wang, Z., Tsoulfas, P., and Blackmore, M.G. (2022). Single nuclei analyses reveal transcriptional profiles and marker genes for diverse supraspinal populations. J. Neurosci. *42*, 8780–8794. https://doi.org/10.1523/JNEUROSCI.1197-22.2022.

86. Roh, H.C., Tsai, L.T.Y., Lyubetskaya, A., Tenen, D., Kumari, M., and Rosen, E.D. (2017). Simultaneous Transcriptional and Epigenomic Profiling from Specific Cell Types within Heterogeneous Tissues In Vivo. Cell Rep. *18*, 1048–1061. https://doi.org/10.1016/j.celrep.2016.12.087.

87. Kishi, T., Aschkenasi, C.J., Choi, B.J., Lopez, M.E., Lee, C.E., Liu, H., Hollenberg, A.N., Friedman, J.M., and Elmquist, J.K. (2005). Neuropeptide Y Y1 receptor mRNA in rodent brain: distribution and colocalization with melanocortin-4 receptor. J. Comp. Neurol. *482*, 217–243. https://doi.org/10.1002/cne.20432.

88. Qi, Y., Lee, N.J., Ip, C.K., Enriquez, R., Tasan, R., Zhang, L., and Herzog, H. (2022). NPY derived from AGRP neurons controls feeding via Y1 and energy expenditure and food foraging behaviour via Y2 signalling. Mol. Metab. *59*, 101455. https://doi.org/10.1016/j.molmet.2022.101455.

89. Atasoy, D., Betley, J.N., Su, H.H., and Sternson, S.M. (2012). Deconstruction of a neural circuit for hunger. Nature *488*, 172–177. https://doi.org/10.1038/nature11270.

90. Vella, K.R., Ramadoss, P., Lam, F.S., Harris, J.C., Ye, F.D., Same, P.D., O'Neill, N.F., Maratos-Flier, E., and Hollenberg, A.N. (2011). NPY and MC4R signaling regulate thyroid hormone levels during fasting through both central and peripheral pathways. Cell Metab. *14*, 780–790. https://doi.org/10.1016/j.cmet.2011.10.009.

91. Harris, M., Aschkenasi, C., Elias, C.F., Chandrankunnel, A., Nillni, E.A., Bjøorbaek, C., Elmquist, J.K., Flier, J.S., and Hollenberg, A.N. (2001). Transcriptional regulation of the thyrotropin-releasing hormone gene by leptin and melanocortin signaling. J. Clin. Investig. *107*, 111–120. https://doi.org/10.1172/JCI10741.

92. Xiao, C., Liu, N., Province, H., Piñol, R.A., Gavrilova, O., and Reitman, M.L. (2020). BRS3 in both MC4R- and SIM1-expressing neurons regulates energy homeostasis in mice. Mol. Metab. *36*, 100969. https://doi.org/10.1016/j.molmet.2020.02.012.

93. Liu, J., Conde, K., Zhang, P., Lilascharoen, V., Xu, Z., Lim, B.K., Seeley, R.J., Zhu, J.J., Scott, M.M., and Pang, Z.P. (2017). Enhanced AMPA Receptor Trafficking Mediates the Anorexigenic Effect of Endogenous Glucagon-like Peptide-1 in the Paraventricular Hypothalamus. Neuron *96*, 897–909.e5. https://doi.org/10.1016/j.neuron.2017.09.042.

94. Geerling, J.C., and Loewy, A.D. (2006). Aldosterone-sensitive neurons in the nucleus of the solitary tract: efferent projections. J. Comp. Neurol. *497*, 223–250. https://doi.org/10.1002/cne.20993.

95. Nectow, A.R., Moya, M.V., Ekstrand, M.I., Mousa, A., McGuire, K.L., Sferrazza, C.E., Field, B.C., Rabinowitz, G.S., Sawicka, K., Liang, Y., et al. (2017). Rapid Molecular Profiling of Defined Cell Types Using Viral TRAP. Cell Rep. *19*, 655–667. https://doi.org/10.1016/j.celrep.2017.03.048.

96. Mogul, A.S., Hadley, C.K., Province, H.S., Pauli, J., Gavrilova, O., Xiao, C., Palmiter, R.D., Piñol, R.A., and Reitman, M.L. (2021). Cre Recombinase Driver Mice Reveal Lineage-Dependent and -Independent Expression of Brs3 in the Mouse Brain. eNeuro *8*, ENEURO.0252-21.2021. https://doi.org/10.1523/ENEURO.0252-21.2021.

97. Daigle, T.L., Madisen, L., Hage, T.A., Valley, M.T., Knoblich, U., Larsen, R.S., Takeno, M.M., Huang, L., Gu, H., Larsen, R., et al. (2018). A Suite of Transgenic Driver and Reporter Mouse Lines with Enhanced Brain-Cell-Type Targeting and Functionality. Cell *174*, 465–480.e22. https://doi.org/10.1016/j.cell.2018.06.035.

98. Hahn, T.M., Breininger, J.F., Baskin, D.G., and Schwartz, M.W. (1998). Coexpression of Agrp and NPY in fasting-activated hypothalamic neurons. Nat. Neurosci. *1*, 271–272. https://doi.org/10.1038/1082.

99. Kc, P., Haxhiu, M.A., Tolentino-Silva, F.P., Wu, M., Trouth, C.O., and Mack, S.O. (2002). Paraventricular vasopressin-containing neurons project to brain stem and spinal cord respiratory-related sites. Respir. Physiol. Neurobiol. *133*, 75–88. https://doi.org/10.1016/s1569-9048(02)00131-3.

100. Oti, T., Satoh, K., Uta, D., Nagafuchi, J., Tateishi, S., Ueda, R., Takanami, K., Young, L.J., Galione, A., Morris, J.F., et al. (2021). Oxytocin Influences Male Sexual Activity via Non-synaptic Axonal Release in the Spinal Cord. Curr. Biol. *31*, 103–114.e5. https://doi.org/10.1016/j.cub.2020.09.089.

101. Papazoglou, I., Lee, J.H., Cui, Z., Li, C., Fulgenzi, G., Bahn, Y.J., Staniszewska-Goraczniak, H.M., Piñol, R.A., Hogue, I.B., Enquist, L.W., et al. (2022). A distinct hypothalamus-to-beta cell circuit modulates insulin secretion. Cell Metab. *34*, 285–298.e7. https://doi.org/10.1016/j.cmet.2021.12.020.

102. Chen, S., and Aston-Jones, G. (1995). Evidence that cholera toxin B subunit (CTb) can be avidly taken up and transported by fibers of passage. Brain Res. *674*, 107–111. https://doi.org/10.1016/0006-8993(95)00020-q.

103. Li, H., Jiang, T., An, S., Xu, M., Gou, L., Ren, B., Shi, X., Wang, X., Yan, J., Yuan, J., et al. (2024). Single-neuron projectomes of mouse paraventricular hypothalamic nucleus oxytocin neurons reveal mutually exclusive projection patterns. Neuron *112*, 1081–1099.e7. https://doi.org/10.1016/j.neuron.2023.12.022.

104. Zhang, B., Qiu, L., Xiao, W., Ni, H., Chen, L., Wang, F., Mai, W., Wu, J., Bao, A., Hu, H., et al. (2021). Reconstruction of the Hypothalamo-Neurohypophysial System and Functional Dissection of Magnocellular Oxytocin Neurons in the Brain. Neuron *109*, 331–346.e7. https://doi.org/10.1016/j.neuron.2020.10.032.

105. Rho, J.H., and Swanson, L.W. (1987). Neuroendocrine CRF motoneurons: intrahypothalamic axon terminals shown with a new retrograde-Lucifer-immuno method. Brain Res. *436*, 143–147. https://doi.org/10.1016/0006-8993(87)91566-6.

106. Fuzesi, T., Daviu, N., Wamsteeker Cusulin, J.I., Bonin, R.P., and Bains, J.S. (2016). Hypothalamic CRH neurons orchestrate complex behaviours after stress. Nat. Commun. *7*, 11937. https://doi.org/10.1038/ncomms11937.

107. Tao, J., Campbell, J.N., Tsai, L.T., Wu, C., Liberles, S.D., and Lowell, B.B. (2021). Highly selective brain-to-gut communication via genetically defined vagus neurons. Neuron *109*, 2106–2115.e4. https://doi.org/10.1016/j.neuron.2021.05.004.

108. Vong, L., Ye, C., Yang, Z., Choi, B., Chua, S., Jr., and Lowell, B.B. (2011). Leptin action on GABAergic neurons prevents obesity and reduces inhibitory tone to POMC neurons. Neuron *71*, 142–154. https://doi.org/10.1016/j.neuron.2011.05.028.

109. Bankhead, P., Loughrey, M.B., Fernández, J.A., Dombrowski, Y., McArt, D.G., Dunne, P.D., McQuaid, S., Gray, R.T., Murray, L.J., Coleman, H.G., et al. (2017). QuPath: Open source software for digital pathology image analysis. Sci. Rep. *7*, 16878. https://doi.org/10.1038/s41598-017-17204-5.

110. Schindelin, J., Arganda-Carreras, I., Frise, E., Kaynig, V., Longair, M., Pietzsch, T., Preibisch, S., Rueden, C., Saalfeld, S., Schmid, B., et al. (2012). Fiji: an open-source platform for biological-image analysis. Nat. Methods *9*, 676–682. https://doi.org/10.1038/nmeth.2019.

111. Dobin, A., Davis, C.A., Schlesinger, F., Drenkow, J., Zaleski, C., Jha, S., Batut, P., Chaisson, M., and Gingeras, T.R. (2013). STAR: ultrafast universal RNA-seq aligner. Bioinformatics *29*, 15–21. https://doi.org/10.1093/bioinformatics/bts635.

112. Fleming, S.J., Chaffin, M.D., Arduini, A., Akkad, A.D., Banks, E., Marioni, J.C., Philippakis, A.A., Ellinor, P.T., and Babadi, M. (2023). Unsupervised removal of systematic background noise from droplet-based single-cell experiments using CellBender. Nat. Methods *20*, 1323–1335. https://doi.org/10.1038/s41592-023-01943-7.

113. Xu, S., Hu, E., Cai, Y., Xie, Z., Luo, X., Zhan, L., Tang, W., Wang, Q., Liu, B., Wang, R., et al. (2024). Using clusterProfiler to characterize multiomics data. Nat. Protoc. *19*, 3292–3320. https://doi.org/10.1038/s41596-024-01020-z.

114. Campbell, J.N., Macosko, E.Z., Fenselau, H., Pers, T.H., Lyubetskaya, A., Tenen, D., Goldman, M., Verstegen, A.M.J., Resch, J.M., McCarroll, S.A., et al. (2017). A molecular census of arcuate hypothalamus and median eminence cell types. Nat. Neurosci. *20*, 484–496. https://doi.org/10.1038/nn.4495.

115. Schwalbe, D.C., Stornetta, D.S., Abraham-Fan, R.J., Souza, G.M.P.R., Jalil, M., Crook, M.E., Campbell, J.N., and Abbott, S.B.G. (2024). Molecular organization of autonomic, respiratory, and spinally-projecting neurons in the mouse ventrolateral medulla. J. Neurosci. *44*, e2211232024. https://doi.org/10.1523/JNEUROSCI.2211-23.2024.

116. Gulko, A., Essene, A., Belmont-Rausch, D.M., Veregge, M., Pant, D., Tenen, D., Kapel, B.S., Emont, M.P., Pers, T.H., Rosen, E.D., and Tsai, L.T. (2024). Protocol for flow cytometry-assisted single-nucleus RNA sequencing of human and mouse adipose tissue with sample multiplexing. STAR Protoc. *5*, 102893. https://doi.org/10.1016/j.xpro.2024.102893.

117. Kowalczyk, M.S., Tirosh, I., Heckl, D., Rao, T.N., Dixit, A., Haas, B.J., Schneider, R.K., Wagers, A.J., Ebert, B.L., and Regev, A. (2015). Single-cell RNA-seq reveals changes in cell cycle and differentiation programs upon aging of hematopoietic stem cells. Genome Res. *25*, 1860–1872. https://doi.org/10.1101/gr.192237.115.

118. Tyssowski, K.M., DeStefino, N.R., Cho, J.-H., Dunn, C.J., Poston, R.G., Carty, C.E., Jones, R.D., Chang, S.M., Romeo, P., Wurzelmann, M.K., et al. (2018). Different Neuronal Activity Patterns Induce Different Gene Expression Programs. Neuron *98*, 530–546.e11. https://doi.org/10.1016/j.neuron.2018.04.001.

119. Boyle, E.I., Weng, S., Gollub, J., Jin, H., Botstein, D., Cherry, J.M., and Sherlock, G. (2004). GO::TermFinder–open source software for accessing Gene Ontology information and finding significantly enriched Gene Ontology terms associated with a list of genes. Bioinformatics *20*, 3710–3715. https://doi.org/10.1093/bioinformatics/bth456.

120. Habib, N., Zhang, F., and Regev, A. (2016). Div-Seq: Single-nucleus RNA-Seq reveals dynamics of rare adult newborn neurons. Science *353*, 922–925. https://doi.org/10.1126/science.aag0863.

121. Todd, W.D., Venner, A., Anaclet, C., Broadhurst, R.Y., De Luca, R., Bandaru, S.S., Issokson, L., Hablitz, L.M., Cravetchi, O., Arrigoni, E., et al. (2020). Suprachiasmatic VIP neurons are required for normal circadian rhythmicity and comprised of molecularly distinct subpopulations. Nat. Commun. *11*, 4410. https://doi.org/10.1038/s41467-020-17197-2.

122. Moffitt, J.R., Bambah-Mukku, D., Eichhorn, S.W., Vaughn, E., Shekhar, K., Perez, J.D., Rubinstein, N.D., Hao, J., Regev, A., Dulac, C., and Zhuang, X. (2018). Molecular, spatial, and functional single-cell profiling of the hypothalamic preoptic region. Science *362*, eaau5324. https://doi.org/10.1126/science.aau5324.

123. Resch, J.M., Fenselau, H., Madara, J.C., Wu, C., Campbell, J.N., Lyubetskaya, A., Dawes, B.A., Tsai, L.T., Li, M.M., Livneh, Y., et al. (2017). Aldosterone-Sensing Neurons in the NTS Exhibit State-Dependent Pacemaker Activity and Drive Sodium Appetite via Synergy with Angiotensin II Signaling. Neuron *96*, 190–206.e7. https://doi.org/10.1016/j.neuron.2017.09.014.

124. Douglass, A.M., Resch, J.M., Madara, J.C., Kucukdereli, H., Yizhar, O., Grama, A., Yamagata, M., Yang, Z., and Lowell, B.B. (2023). Neural basis for fasting activation of the hypothalamic-pituitary-adrenal axis. Nature *620*, 154–162. https://doi.org/10.1038/s41586-023-06358-0.

STAR★METHODS

KEY RESOURCES TABLE

REAGENT or RESOURCE	SOURCE	IDENTIFIER
Antibodies		
Rabbit anti-Fluoro-Gold	Milipore Sigma	Cat#: AB153-I; RRID:AB_90738
Goat polyclonal anti-cholera toxin subunit B	List Biological Laboratories	Cat#: 703; RRID:AB_10013220
Rabbit polyclonal anti-GFP	Thermo Fisher Scientific	Cat#: A-11122; RRID:AB_221569
Rat monoclonal anti-mCherry	Thermo Fisher Scientific	Cat#: M11217; RRID:AB_2536611
Bacterial and virus strains		
AAVDJ-hSyn-H2B-mCherry	Boston Children's Hospital Viral Core; Tao et al.[107]	NA
AAVrg-hSyn-Cre	Addgene; Donating Investigator: James M. Wilson	Addgene: 105553
AAVrg-CAG-GFP-Cre	Boston Children's Hospital Viral Core	NA
HSV-hEf1a-mCherry-IRES-Cre	Mass General Brigham Gene Delivery Technology Core; Dr. Rachael Neve	NA
AAV5-EF1a-FLEX-EGFP-L10a	Addgene; Donating Investigators: Nathaniel Heintz & Alexander Nectow & Eric Schmidt	Addgene: 98747
AAVDJ-hSyn-DIO-EGFP-TeTxLC	ETH Zurich Viral Vector Facility	v322-5
AAV8-hSyn-DIO-EGFP	Addgene; Donating Investigator: Bryan Roth	Addgene: 50457
AAV8-hSyn-DIO-mCherry	Addgene; Donating Investigator: Bryan Roth	Addgene: 50459
AAV5-EF1a-fDIO-ChR2-eYFP	UNC viral vector core	172055
AAV9-EF1a-DIO-ChR2-eYFP	Addgene; Donating Investigator: Karl Deisseroth	Addgene: 20298
AAV9-EF1a-DIO-ChR2-mCherry	Addgene; Donating Investigator: Karl Deisseroth	Addgene: 20297
AAVrg-hSyn-mCherry	Addgene; Donating Investigator: Karl Deisseroth	Addgene: 114472
Chemicals, peptides, and recombinant proteins		
Cholera Toxin Subunit B	List Biological Laboratories	Cat#: 104
Fluoro-Gold	Fluorochrome	NA
10% phosphate-buffered formalin	Fisher	CAT#: SF100-20
Tissue-Tek® O.C.T. Compound	Sakura	Product code: 4583
Paraformaldehyde	Electron Microscopy Sciences	CAT#: 15714-S
RNase-free PBS, pH 7.4	Thermo Fisher Scientific	CAT#: AM9625
ammonium persulfate	Sigma	CAT#: 09913-100G
TEMED	Sigma	CAT#: T7024-25ML
Protease K	New England Biolabs	CAT#: P8107S
Barcoded Oligo dT primer ON Beads	Chemgenes	Cat#: Macosko-2011-10
Opal Dye 570 Reagent Pack	Akoya Biosciences	CAT#: FP1488001KT
Opal Dye 650 Reagent Pack	Akoya Biosciences	CAT#: FP1496001KT
Opal Dye 780 Reagent Pack	Akoya Biosciences	CAT#: FP1501001KT
Critical commercial assays		
RNAscope Multiplex Fluorescent Reagent Kit V2	Advanced Cell Diagnostics	CAT#: 323100
MERSCOPE Instrument	Vizgen	CAT#: 10000001
MERSCOPE Sample Prep Kit	Vizgen	CAT#: 10400012
MERSCOPE 500 Gene Imaging Kit	Vizgen	CAT#: 10400006

(*Continued on next page*)

Continued

REAGENT or RESOURCE	SOURCE	IDENTIFIER
Chromium Next GEM Single Cell 3′ GEM Kit v3.1	10X Genomics	PN-1000269
Chromium Next GEM Chip G Single Cell Kit	10X Genomics	PN-1000120
Deposited data		
Raw and analyzed PVH sequencing data	This paper	GEO: GSE303256
Mouse PVH MERFISH data	This paper	Iowa Research Online IRO: 9984403060302771
Deposited code and Robjects	This paper	https://zenodo.org/records/15983704
Allen Brain Cell Atlas Hypothalamic 10Xv2 data	Yao et al.[29]	https://allen-brain-cell-atlas.s3.us-west-2.amazonaws.com/index.html#expression_matrices/WMB-10Xv2/20230630/
Allen Brain Cell Atlas Hypothalamic 10Xv3 data	Yao et al.[29]	https://allen-brain-cell-atlas.s3.us-west-2.amazonaws.com/index.html#expression_matrices/WMB-10Xv3/20230630/
Spinal cord-projecting PVH data from Winter et al.	Winter et al.[84]	GEO: GSE247594
Spinal cord-projecting PVH data from Beine et al.	Beine et al.[85]	GEO: GSE212409
Human PVH snRNA-seq data from Siletti et al.	Siletti et al.[70]	https://datasets.cellxgene.cziscience.com/5e399d37-23d3-4673-8761-9f443c1fdc14.rds
Human PVH snRNA-seq data from Tadross et al. (“HYPOMAP”)	Tadross et al.[71]	https://www.repository.cam.ac.uk/items/cad1c61a-e4e5-4443-ad11-92e4f48b3861
Experimental models: Organisms/strains		
Mouse: C57BL/6J	The Jackson Laboratory	JAX: 000664
Mouse: *Sim1*-Cre	Balthasar et al.[14]	JAX: 006395
Mouse: R26-LSL-EGFP-L10a	Krashes et al.[22]	MGI: 5559562
Mouse: H2B-TRAP	Roh et al.[86]	JAX: 029789
Mouse: *Brs3*-IRES-Cre	Mogul et al.[96]	JAX: 030540
Mouse: *Npy*-IRES-Flp	Daigle et al.[97]	JAX: 030211
Mouse: *Slc17a6*-IRES-Cre	Vong et al.[108]	JAX: 028863
Mouse: *Slc32a1*-IRES-Cre	Vong et al.[108]	JAX: 028862
Mouse: *Mc4r*-2a-Cre	Garfield et al.[12]	JAX: 030759
Oligonucleotides		
Mm-Aox3-C1	Advanced Cell Diagnostics	CAT#: 836451
Mm-Avp-C3	Advanced Cell Diagnostics	CAT#: 401391-C3
Mm-Brs3-C1	Advanced Cell Diagnostics	CAT#: 454111
Mm-Brs3-C3	Advanced Cell Diagnostics	CAT#: 454111-C3
Mm-Col12a1-C2	Advanced Cell Diagnostics	CAT#: 312631-C2
Mm-Crh-C1	Advanced Cell Diagnostics	CAT#: 316091
Mm-Esr2-C3	Advanced Cell Diagnostics	CAT#: 316121-C3
Mm-Nfix-C2	Advanced Cell Diagnostics	CAT#: 522331-C2
Mm-Npr3-C2	Advanced Cell Diagnostics	CAT#: 502991-C2
Mm-Npsr1-C1	Advanced Cell Diagnostics	CAT#: 317501
Mm-Oxt-C2	Advanced Cell Diagnostics	CAT#: 493171-C2
Mm-Pla2r1-No-XHs-C1	Advanced Cell Diagnostics	CAT#: 854581
Mm-Rxfp3-C1	Advanced Cell Diagnostics	CAT#: 439381
Mm-Scgn-C2	Advanced Cell Diagnostics	CAT#: 482721-C2
Mm-Sim2-C1	Advanced Cell Diagnostics	CAT#: 1108911
Mm-Sst-C1	Advanced Cell Diagnostics	CAT#: 404631
Mm-Trh-C1	Advanced Cell Diagnostics	CAT#: 436811

(*Continued on next page*)

Continued

REAGENT or RESOURCE	SOURCE	IDENTIFIER
Software and algorithms		
Original code and Seurat objects	This paper	https://doi.org/10.5281/zenodo.15983704
Cellpose2	Pachitariu et al.[50]	https://www.cellpose.org/
QuPath	Bankhead et al.[109]	https://qupath.github.io/
ImageJ	Schindelin et al.[110]	https://imagej.net/software/imagej/
Affinity Designer	Affinity	RRID:SCR_016952
R v4.4.1	The R Foundation	https://www.r-project.org/; RRID: SCR_001905
Rstudio	RStudio, PBC	https://posit.co/blog/rstudio-pbc/
Vpt	Vizgen	https://vizgen.github.io/vizgen-postprocessing/index.html
Bcl2fastq v2.20.0	Illumina	https://support.illumina.com/sequencing/sequencing_software/bcl2fastq-conversion-software.html; RRID: SCR_015058
Drop-Seq tools v2.3.0	Broad Institute	https://github.com/broadinstitute/Drop-seq; RRID:SCR_018142
STAR v2.7.7 and v2.6.1	Dobin et al.[111]	https://github.com/alexdobin/STAR;
CellRanger v6.1.2 and v7.0.1	10X Genomics	http://www.10xgenomics.com/
Seurat v5.0.1.9001	Hao et al.[35]; Stuart et al.[36]	https://satijalab.org/seurat/; RRID:SCR_016341
CellBender v0.2.0	Fleming et al.[112]	https://github.com/broadinstitute/CellBender
clusterProfiler v4.12.6	Xu et al.[113]	https://bioconductor.org/packages/release/bioc/html/clusterProfiler.html; RRID:SCR_016884
SpaDo v1.2.0	Duan et al.[51]	https://github.com/bm2-lab/SpaDo
Picard Tools v2.18.21	Broad institute	http://broadinstitute.github.io/picard/; RRID:_SCR_006525
Prism 10	GraphPad Sowtware	https://www.graphpad.com/; RRID:SCR_000306

EXPERIMENTAL MODEL AND STUDY PARTICIPANT DETAILS

Mice

All animal care and experimental procedures were approved by the Institutional Animal Care and Use Committees at Beth Israel Deaconess Medical Center (047–2022) and the University of Iowa (3102343). Prior to the start of experiments, mice were housed in a temperature- and humidity-controlled room with a 12-h light-dark cycle and *ad libitum* access to water and standard diet (Inotiv 7913) unless stated otherwise. C57BL/6J background wild-type mice aged 6–12 weeks were used for the majority of single-cell and single-nucleus RNA sequencing experiments, while MERFISH experiments were performed with 8–10-week-old C57BL/6J mice. In some cases, *Sim1*-Cre (JAX:006395),[14] *Sim1*-Cre::R26-LSL-EGFP-L10a,[22] or H2B-TRAP mice (JAX:029789)[86] were used for single-cell and single-nucleus RNA sequencing studies to guide dissections and sample collection with FANS. Behavioral experiments were conducted with *Brs3*-IRES-Cre mice (JAX030540),[96] which were crossed to *Npy*-IRES-Flp (JAX:030211)[97] mice for CRACM experiments. Additionally, *Slc17a6*-IRES-Cre (JAX:028863)[108]::R26-LSL-EGFP-L10a,[22] *Slc32a1*-IRES-Cre (JAX:028862)[108]::R26-LSL-EGFP-L10a, *Mc4r*-2a-Cre (JAX:030759),[12] and C57BL/6J wild-type mice were used for histological experiments. All mice used were hemizygous or heterozygous for genetic modifications. For stereotaxic surgeries, mice were 6–10 weeks old at the time of injection. All experiments were conducted with both males and females, except those using *Brs3*-IRES-Cre mice, which used only males, limiting our ability to extend our findings to females in food intake and body weight studies. No sex-dependent effects were observed in sc/snRNA sequencing and MERFISH analyses.

METHOD DETAILS

Single-cell/nucleus RNA sequencing tissue collection, library preparation, and sequencing

C57BL/6J, *Sim1*-Cre, or *Sim1*-Cre::R26-LSL-EGFP-L10a mice aged 6–12 weeks were sacrificed between 9 a.m.–12 p.m. by rapid decapitation immediately after removal from the home cage. Brains were extracted and chilled in DMEM/F12 media slush. Next,

brains were placed ventral side up in a chilled stainless steel brain matrix (Roboz Surgical Instrument Co.: SA-2165), and 1 mm coronal sections of the hypothalamus were collected. The PVH was then micro-dissected under a fluorescent stereoscope. For each sample preparation, 4–10 male or female mice were pooled. Sample and library preparation was performed as described previously for Drop-seq[114] and DroNc-seq[46] with minor modifications. One of three DroNc-seq samples was prepared from fasted C57BL/6J mice. For 10X Chromium v3 sequencing runs, samples and library preps were prepared as described previously for incorporation with fluorescence-activated nuclei sorting (FANS) with minor modifications.[115,116] In addition, subsets of 10X Chromium v3 samples from *Sim1*-Cre mice injected with AAVDJ-hSyn-H2B-mCherry (Boston Children's Hospital Viral Core)[107] or H2B-TRAP mice injected with AAVrg-hSyn-Cre, for projection-specific snRNA-seq experiments described below, were incubated with hashtag oligos (TotalSeq-A, BioLegend) for 15 min for eventual multiplexing prior to FANS enrichment based on nuclear mCherry. Multiplexed *Sim1*-Cre samples were obtained from mice that were *ad libitum* fed, fasted, or refed for 60 min before sacrifice. Libraries were sequenced on an Illumina NextSeq 500 or Illumina NovaSeq 6000 at a minimum read depth of 20,000 reads per cell/nucleus. Hashtag oligo libraries were sequenced to a minimum read depth of either 1,000 or 5,000 reads/nucleus and processed into count matrices using either the Cumulus Tool on Feature Barcoding (https://github.com/lilab-bcb/cumulus_feature_barcoding) or kallisto | bustools (https://www.kallistobus.tools/). For Drop-seq and DroNc-seq data, raw sequencing reads were processed using the Drop-seq tools pipeline.[46,114] Barcodes with base quality <10 were removed, and 5′ and 3′ ends of reads were trimmed to remove TSO and poly(A) tails, respectively. Reads were then aligned to the GRCm38 reference genome using STAR v2.7.7.[111] Feature-barcode matrices were then generated by summing detected unique molecular identifiers (UMIs) for each barcode with errors corrected at a hamming distance of 1. For 10X Chromium v3 libraries, 10X Genomics Cell Ranger was used to map reads to the GRCm38 reference genome and generate feature-barcode matrices.

Single-cell/nucleus RNA sequencing quality control

For all sequencing data regardless of technology, CellBender (v0.2.2) was used to identify and filter out reads captured from ambient RNA and random barcode swapping.[112] Subsequently, data from Drop-seq, DroNc-seq, and 10X Chromium v3 sequencing runs were loaded into an RStudio environment (R v4.4.1) and processed through a custom Seurat-based analysis pipeline run in Seurat v5.0.1.9001.[35] First, we applied additional filtering to remove cells/nuclei with fewer than 250 unique genes. DroNc-seq data were then filtered to exclude nuclei with total UMI count outside the range of 1,000 to 10,000, while Drop-seq and 10X Chromium-v3 data were filtered to exclude cells/nuclei with total UMI count outside the range of 1,000 to 25,000. Additionally, *PercentFeatureSet*() was used to calculate mitochondrial gene expression, and cells/nuclei from all datasets were removed if they had a mitochondrial gene expression rate of greater than 10%. Finally, all cells/nuclei with a ratio of $\log_{10}$(unique genes)/$\log_{10}$(unique molecules) less than 0.8 were removed. After quality control filtering was complete, all data were merged into a single Seurat object for integrated analysis.

Single-cell/nucleus RNA sequencing and data integration

For integrated analysis, 11 batches of sequencing runs were merged into a single Seurat object (Drop-seq = 7 batches, DroNc-seq = 2 batches, and 10X Chromium-v3 = 2 batches) followed by joining of the "RNA" assay layers using *JoinLayers()*. Raw counts were log-normalized, using Seurat *NormalizeData()*, and cell cycle scoring for S phase and G2/M was computed using the Seurat *CellCycleScoring()* function.[117] Subsequently, given that stress readily activates PVH neurons, particularly PVH^{Crh} neurons controlling the HPA axis, the *AddModuleScore()* function was used to measure the expression level of a set of 19 primary rapidly responding activity-dependent genes to compute a "cellular activation score" based on this transcriptional signature for each cell.[118] Next, layers were split by sequencing run ("batch"), and *FindVariableFeatures()* was used to select the top 5,000 highly variable genes. Data were then scaled with *ScaleData()*, while regressing out the following covariates: mitochondrial gene percentage, cell-cycle scores, and cellular activation score. Principal component analysis (PCA) was performed with the *RunPCA()* function. Following calculation of principal components, integration of layers was carried out using *IntegrateLayers()* with reciprocal principal component analysis (RPCA)-based integration.[36] After integration, we used the top 30 principal components for clustering and dimensionality reduction using the Seurat *FindNeighbors()*, *FindClusters(),* and *RunUMAP()* functions. To identify marker genes for each cluster, we re-joined layers using *JoinLayers()* and ran *FindAllMarkers()* for differential gene expression analysis (DGEA) using the non-parametric *Wilcoxon Rank-Sum test*. Differentially expressed genes were defined as those with >0.2 average $\log_2$ fold change and a *Bonferroni-corrected p*-value less than 0.01. Marker gene analysis guided identification of doublets/multiplets, which were classified as clusters that expressed high levels of more than one canonical cell type marker genes (e.g., clusters expressing marker genes for both neurons and astrocytes) and were removed. In addition, clusters comprised of "low quality" metrics, including mitochondrial gene enrichment or absence of cell type-defining markers indicating low complexity, were removed. This process was repeated at several levels of analysis, beginning with all cells, then after subclustering for neurons, GABAergic neurons, glutamatergic neurons, and *Sim1*-expressing neurons.

Integration of *Sim1*-expressing clusters with publicly available HypoMap and Allen Brain Cell Atlas data

To integrate *Sim1*$^+$ PVH sc/snRNA-seq data from our study with publicly available sequencing data from the murine PVH, we downloaded data from HypoMap, an integrated atlas of mouse hypothalamus.[32] Using the provided anatomical annotations with the Seurat object, we subset for and clustered only cells/nuclei annotated as "paraventricular hypothalamic nucleus" using the pipeline

described for this study. Notably, during clustering, we curated the HypoMap data for *Sim1*-expressing cells/nuclei, filtering out any clusters marked by specific expression of GABAergic or thalamic marker genes (i.e., *Slc32a1* and *Tcf7l2*). We then merged and integrated the HypoMap PVH *Sim1*$^+$ neurons with PVH *Sim1*$^+$ sc/snRNA-seq data collected in this study using our Seurat-based analysis workflow. However, after integration, inconsistencies were observed across datasets. We then instead integrated publicly available PVH *Sim1*$^+$ scRNA-seq data from the whole mouse brain Allen Brain Cell (ABC) Atlas with *Sim1*$^+$ PVH sc/snRNA-seq data from this study.[29] To specifically access PVH cells from the ABC Atlas, we first downloaded two H5 AnnData expression matrices (WMB-10Xv2-Hy-raw.h5ad and WMB-10Xv3-Hy-raw.h5ad) containing all cells collected from hypothalamic dissections and sequenced using either 10X Chromium v2 or 10X Chromium v3 chemistry. Subsequently, we used the *Convert()* and *LoadH5Seurat()* functions to load the ABC Atlas data into a Seurat object and used the published taxonomic classifications to select for data from the PVH region. The ABC Atlas assigned anatomical annotation was used to specifically select clusters that spatially mapped to either the PVH (''PVH'') or the anterior portion of the periventricular area (''PVa''). Subsequently, we further filtered our selection only to keep glutamatergic clusters using the ABC Atlas assigned neurotransmitter type label, keeping clusters annotated as either ''Glut'' or ''Glut-GABA''. We then removed cells with a mitochondrial gene expression rate greater than 10% and clustered the data in Seurat version 5. For clustering, ABC Atlas data were processed as described above with minor modifications. Notably, the 10X chemistry (i.e., v2 and v3) were each treated as a ''batch'' for integrated analysis. After clustering, any identified ''low quality'' or doublet/multiplet clusters were removed as described above. Finally, we merged and integrated the ABC Atlas *Sim1*$^+$ neurons with the PVH *Sim1*$^+$ sc/snRNA-seq data from this study following the workflow described above.

Analysis of neuroendocrine neuron transcriptional profiles

DGEA was run using Seurat *FindMarkers()* on the different neuron classes: centrally-projecting, neuroendocrine, median eminence-projecting, and posterior pituitary-projecting neurons. Differentially expressed genes were defined as having >0.2 average $\log_2$ fold change and a *Bonferroni-corrected p*-value <0.01. Next, the clusterProfiler package was used to perform Gene Ontology (GO) enrichment analysis of genes differentially expressed by centrally-projecting, neuroendocrine, median eminence-projecting, and posterior pituitary-projecting neuronal classes.[113] Specifically, *compareCluster()* was used to perform ''enrichGO'' analysis, which executes an over-representation analysis[119] for all GO ontology categories (i.e., biological process, cellular component, and molecular function) with *Bonferroni correction* for multiple comparisons at an alpha value of 0.05.

Single-nucleus RNA sequencing of projection-specific PVH neuron populations

We sequenced projection-specific PVH neurons using either 10X Chromium v3 or Smart-Seq2 (''sNuc-seq'')[120,121] technologies. For 10X Chromium v3 experiments, H2B-TRAP mice received bilateral stereotaxic injections of AAVrg-hSyn-Cre (Addgene #105553) into either the upper thoracic spinal cord or the parabrachial region. sNuc-seq samples were prepared by bilaterally injecting C57BL/6J mice with AAVDJ-hSyn-DIO-H2B-mCherry into the PVH and AAVrg-CAG-GFP-Cre (Boston Children's Hospital Viral Core) or HSV-hEf1a-mCherry-IRES-Cre (Mass General Brigham Gene Delivery Technology Core; Dr. Rachael Neve) into the PB. Two weeks post-surgery, animals were sacrificed, and tissue was collected as described above. Samples processed with 10X Chromium v3 were completed as described in Schwalbe et al.,[115] while sNuc-seq was performed as described in Tao et al.[107] Spinal cord-projecting data consists of two 10X Chromium v3 sequencing runs, while the parabrachial-projecting data consists of two runs of 10X Chromium v3 and two sNuc-Seq sequencing runs. In addition, we downloaded two publicly available spinal cord-projecting datasets (GEO: GSE247594 and GSE212409)[84,85] and accordingly classified these data using our *Sim1*$^+$ PVH sc/snRNA-seq reference atlas. Briefly, we calculated the percentage of mitochondrial gene expression using Seurat's *PercentFeatureSet()* to identify and remove any cells/nuclei with a mitochondrial gene expression rate greater >10%. Cells/nuclei with fewer than 1000 UMIs were also removed from further analysis. Subsequently, we clustered all parabrachial- and spinal cord-projecting data using the analysis pipeline described above and filtered the data to only retain *Sim1*-expressing clusters. To classify each cell, we proceeded to use *FindTransferAnchors()* to project our mouse *Sim1*$^+$ sc/snRNA-seq reference atlas PCA structure onto the parabrachial- and spinal cord-projecting data to identify paired anchor cells across datasets. We then used the identified anchors and the *MapQuery()* function to map parabrachial- and spinal cord-projecting data into our mouse *Sim1*$^+$ sc/snRNA-seq reference atlas UMAP space.

Analysis of human PVH single-nucleus RNA sequencing data

Two published datasets contain snRNA-seq data from the hypothalamus of adult humans.[70,71] From Siletti et al., 2023,[70] we downloaded a Seurat object containing data from dissections encompassing the medial preoptic region of the hypothalamus, supraoptic region of the hypothalamus, and paraventricular nucleus of the hypothalamus. We then filtered the data for neurons with >1,000 UMIs and <10% mitochondrial gene expression and retained *SIM1*$^+$ clusters for further analysis. After filtering for *SIM1*$^+$ neurons, the data included samples from one 60-year-old female and one 50-year-old male. We also downloaded a Seurat object from Tadross et al., 2025,[71] containing data from the entire adult human hypothalamus, which was filtered as above and contributed data from two females, aged 63 and 94 years, and four males, aged 83, 88, 91, and 94. After analyzing the integrated human *SIM1*$^+$ data, we used a text file (''gene_ortologs.gz'') available from NCBI (https://ftp.ncbi.nlm.nih.gov/gene/DATA/) to identify all gene homologs present in both the human *SIM1*$^+$ object and our mouse *Sim1*$^+$ sc/snRNA-seq atlas. We then completed a canonical correlation analysis (CCA) to assess the transcriptional similarity of each cluster between the human and mouse atlases by using Seurat's *FindTransferAnchors*() and *TransferData*() functions.

MERFISH gene panel selection

A gene panel of 503 genes (Table S6) was curated specifically for the PVH and surrounding regions based on differentially expressed genes identified in sc/snRNA-seq experiments (Tables S1, S2, and S4), canonical marker genes for neurons and non-neuronal cells, and functionally important genes described in the scientific literature. After gene selection, Vizgen manufactured the custom "MERFISH 500 Gene Panel" (Vizgen: 20300008), comprised of probes targeting a minimum of 30 regions per gene (except for *Avp* and *Oxt*) and using a 25-bit binary code readout for gene assignment after combinatorial single molecule FISH (smFISH). Furthermore, 50 "blanks" comprising non-encoding scrambled sequences were included in the gene panel as negative controls (Table S7). Three of the 503 genes, *Avp*, *Oxt*, and *Sst*, were assigned to the "sequential panel" to avoid optical overcrowding artifacts due to high abundance of expression. Genes in the sequential panel are detected using unique probes identified by their direct fluorescent signal in distinct imaging rounds occurring after combinatorial smFISH imaging.

MERFISH tissue collection and sample preparation

MERFISH experiments were conducted according to Vizgen MERSCOPE protocols for fresh frozen tissue using six C57BL/6J mice, comprised of four males and two females, aged 8–10 weeks. Sacrifice and brain extraction was done as described for sc/snRNA-seq studies above. Brains were then positioned ventral side up in a chilled stainless steel brain matrix and sliced into 3-mm thick coronal slices that included the PVH region. Subsequently, the coronal slices were placed anterior side up and trimmed dorsally, removing tissue above the lateral septum, and laterally to remove cortex and much of the striatum. PVH tissue blocks were then embedded in a square mold (S22, Kisker Biotech) with Tissue-Tek O.C.T. Compound (Sakura, 4583) and stored at −80°C until sectioning. Tissue blocks were placed in a cryostat (Epredia CryoStar NX50 HD Cryostat) and incubated at −20°C for 1 h prior to sectioning coronally at 10 μm thickness. We mounted 4-10 sections from each brain at ∼100 μm intervals onto warm MERSCOPE slides (Vizgen: 20400001), beginning at approximately bregma level −0.4 mm and continuing to −1.2 mm according to the Franklin-Paxinos atlas.[49] After sectioning, MERFISH slides were placed face-up in a 60 mm Petri dish (VWR, 25382-687) and left at room temperature for 5 min. Next, slides were incubated in freshly made 4% paraformaldehyde (PFA; Electron Microscopy Sciences: 15714-S) in RNase-free phosphate-buffered saline (PBS, pH 7.4; Thermo Fisher Scientific: AM9625) for 15 min at room temperature. Slides were then washed three times for five minutes each with PBS at room temperature and treated with freshly made 70% ethanol for tissue permeabilization and storage for a minimum of 24 h at 4°C in parafilm-sealed 60 mm dishes.

MERFISH probe hybridization and imaging

Sample preparation was performed using the MERSCOPE Sample Preparation Kit (Vizgen, Cat# 10400012) according to the manufacturer's protocol. Slides were taken out of 4°C and washed with Sample Preparation Wash Buffer for five minutes at room temperature, followed by incubation in Formamide Wash Buffer for 30 min at 37°C. Subsequently, our custom 503 gene MERSCOPE panel for the PVH was applied to the slides with a parafilm coverslip and incubated at 37°C for 36–42 h. Slides were then washed twice with Formamide Wash Buffer for 30 min each at 47°C. To gel-embed tissue samples on slides, a mix composed of Vizgen Gel Embedding Premix, ammonium persulfate (APS; Sigma: 09913-100G), and TEMED (Sigma: T7024-25ML) was prepared and applied to the tissue. A circular Gel Coverslip, treated with RNaseZap, 70% ethanol, and Gel Slick Solution, was then placed on the slide over the gel embedding solution. Gel embedding solution was allowed to solidify for 90 min, after which the coverslip was removed. The sample was then incubated at 37°C in Clearing Solution, comprised of Protease K (New England Biolabs: P8107S) and Vizgen Clearing Premix, for a minimum of 24 h and up to five days prior to imaging.

Imaging was performed using the MERSCOPE 500 Gene Imaging Kit (Vizgen, Cat# 10400006) following the manufacturer's protocol. On the day of imaging, the slides were washed twice with Sample Preparation Wash Buffer at room temperature and treated with DAPI and PolyT Staining Reagent for 15 min on a rocker. The slides were then washed with Formamide Wash Buffer for 15 min, followed by a final wash with Sample Prep Wash Buffer. To begin the imaging process, an individual slide was assembled into the MERSCOPE Flow Chamber and inserted into the instrument along with a MERSCOPE 500 Gene Imaging Cartridge that was activated by Vizgen Imaging Buffer Activator mixed with RNase Inhibitor (New England Biolabs: M0314L). After defining the regions of interest on the slide within the Vizgen MERSCOPE Instrument software, we started the fully automated instrument run. The MERSCOPE Instrument Software automatically processed the raw images to generate spatial genomics data ready for downstream analysis. Although MERFISH was successful, Slides 3 and 6 underwent unsuccessful Vizgen MERSCOPE protein staining, and these protein staining results were excluded from downstream analyses.

MERFISH image analysis and cell segmentation

After image acquisition, the data were initially processed by Vizgen MERSCOPE Instrument Software, before custom cell segmentation was performed with the deep learning algorithm, Cellpose 2.0,[50] using DAPI and PolyT-stained images as training files. First, we uploaded a field of view from one PVH section (Slide 3, bregma level −0.8) as an initial training image. Next, we employed the generalizable 'cyto2' model in Cellpose 2.0 with a diameter parameter of 123.73 pixels to initially segment various cell types in the PVH and surrounding regions. Manual annotations were then adjusted by correcting misidentified cells and adding cells missed by the automated 'cyto2' model. This process was repeated for 10 fields of view, and the new set of 10 human-processed images were used to optimize the training of our custom Cellpose 2.0 segmentation model. This enhanced model was then utilized to segment cells in all Z planes across 41 coronal sections using the Vizgen Post-processing Tool (VPT). All regions underwent

7-layer segmentation, except for the section corresponding to bregma level −0.7 mm on Slide 2, which underwent segmentation with 6 layers of DAPI and PolyT images due to the loss of the DAPI image from layer 3 during data transfer. Four output files were generated for each coronal section: 1) cellpose2_micron_to_mosaic.parquat (cell boundaries file); 2) cell_by_gene.csv (cell by gene matrix)l; 3) detected_transcripts.csv (cartesian coordinates of each transcript); and 4) cell_metadata.csv (cell morphology characteristics).

MERFISH sequential gene panel preprocessing

Due to high-expression levels within the PVH, *Avp*, *Oxt*, and *Sst* expression was assayed with a non-combinatorial sequential gene panel as noted above. Using the VPT sum_signal command on data segmented by Cellpose 2.0, we generated summed fluorescent values for *Avp*, *Oxt*, and *Sst* for each cell in our MERFISH study. We then performed a volume-based normalization of the fluorescent signals using a modified version of previously published methods.[122] Specifically, we first took the High_pass fluorescent values for *Avp*, *Oxt*, and *Sst* for each cell and divided each value by the cell's volume to yield volume-normalized fluorescence values. Subsequently, we subtracted the respective median volume-normalized fluorescence value for *Avp*, *Oxt*, and *Sst* from all cells and set any negative values to 0. Finally, we divided our median-subtracted, volume-normalized fluorescence value by 1,000 and appended the resulting values for *Avp*, *Oxt*, and *Sst* expression to the cell_by_gene matrix.

MERFISH data analysis

VPT output files were loaded as Seurat objects in an R Studio environment (R v4.4.1) (Seurat v5.0.1.9001) using the Seurat *LoadVizgen()* function. Data from all 41 sections were then merged into one MERFISH Seurat object. Next, we defined the region of interest (ROI) for each section by selecting the rectangular area 200 μm dorsal, 1000 μm ventral, and 700 μm lateral to the top of the third ventricle. The unique IDs for all cells within each ROI detected in *z*-plane three were exported to a .csv file using the Vizgen MERSCOPE Visualizer. The merged MERFISH Seurat object was then subset to retain only cells within our defined ROIs. Subsequently, all cells with less than 15 gene counts were removed, and the remaining cells were analyzed with the Seurat-based pipeline described above, with minor modifications. Notably, *i)* during *FindVariableFeatures()*, clip. range was set to "(-10, 10)", according to Seurat recommendations for analyzing FISH-based counts, *ii)* no covariates were regressed during scaling of variable features, and *iii)* PCA was conducted with only the combinatorial smFISH features, excluding mCherry. As with sc/snRNA-seq, the merged Seurat MERFISH object was split by ROI ("Slide_ID") after running PCA, and we subsequently performed a reciprocal principal component analysis (RPCA)-based integration[36] with Seurat *IntegrateLayers()* to correct for any batch effects. After integration, multiplet clusters driven by inaccurate cell segmentation were removed, and the post-integration steps in our pipeline were repeated until no multiplet clusters were observed. For differential gene expression analysis, we joined layers and ran *FindAllMarkers()* using the non-parametric *Wilcoxon Rank-Sum test*. Differentially expressed genes were defined as those >0.2 average $\log_2$ fold change and a *Bonferroni-corrected p*-value <0.01. The post-integration pipeline was run for all levels of subclustering, beginning with all cells, followed by analysis of *Slc17a6*$^+$/*Sim1*$^+$, *Slc17a6*$^+$/*Sim1*$^-$, and *Slc32a1*$^+$ populations.

MERFISH spatial domain analysis

After cell-type clustering with Seurat, we performed a multi-slice spatial domain detection analysis using the R package SpaDo.[51] Due to computational processing limitations, the initial analysis was limited to data from three animals (two male and one female), which had the most extensive rostral-to-caudal coverage of the PVH region and included 25 out of the total 41 tissue slices of the MERFISH analysis. Specifically, we selected slices spanning bregma levels −0.4 mm to −1.2 mm from Slides 3, 4, and 5. Spatial domain analysis was performed by using the *SpatialCellTypeDistribution_multiple()* function to calculate the Spatially Adjacent Cell type Embedding (SPACE) for the MERFISH data. SPACE is calculated via a k-nearest neighbor analysis that identifies a cell's local niche, which is then integrated with its cell-type annotation derived from the Seurat analysis. Once SPACE was computed, we used the *DistributionDistance()* function to assess similarities between local niches, quantified by Jensen-Shannon divergence (JSD). Subsequently, the *DomainHclust()* function was used with 'auto_resolution' set to 1, to derive spatial domains across all included cells and tissue sections. We then imported the calculated spatial domain information into Seurat as metadata to facilitate figure generation. Finally, to allow visualization of spatial domains across all tissue slices, we leveraged the results from this initial analysis to perform reference-based spatial domain annotation of the remaining 16 tissue slices. To accomplish this, we used the *SpatialReference()* and *SpatialQuery()* functions to assign spatial domain annotations to a query dataset based on JSD-distance between the SPACE of each cell in the query dataset and the SPACE centroid for each domain in the reference dataset (Figure S6A).

Stereotaxic injections and optic fiber implantation

Mice aged 6–10 weeks were deeply anesthetized by intraperitoneal injection of a ketamine/xylazine cocktail (100 mg/kg ketamine; 10 mg/kg xylazine). Next, the surgical area was shaved and sterilized prior to placing the mouse into a stereotactic frame (David Kopf model 940). For spinal cord injections, a midline incision was made above the interscapular region. Vertebrae were visualized by blunt dissection, and T2 was used to identify the injection site location between T2 and T3. The dorsal part of one vertebra was removed with forceps, allowing access to the spinal cord for injection. Injections were made ±0.4 mm lateral to the midline by lowering a pulled glass pipette containing adeno-associated virus (AAV) or retrograde tracer (Fluoro-Gold or cholera toxin subunit B) into the spinal cord and using an air pressure injection system controlled by a Grass S48 stimulator to control injection speed.[123] Spinal cord

injections began at −0.9 mm ventral to the surface of the spinal cord, and AAV/tracer continued to be injected while slowly raising the glass pipette to −0.2 mm. At the completion of each injection, the pipette was left in place for five minutes before removal. This process was then repeated on the contralateral side. To close the incision, the muscle layer was sutured with absorbable sutures (MedVet International: JORG22419), and the skin was sutured with non-absorbable sutures (MedVet International: MV-8661-V). For brain injections, a midline incision was made to expose the skull. At the site of injection, a small hole was drilled, and a pulled glass micropipette containing AAV or retrograde tracer was lowered to the desired injection site depth before infusions commenced using the air pressure injection system described above. Stereotactic coordinates for brain injections were as follows (from bregma): PVH, posterior −0.85, lateral ±0.2, and ventral −4.9; PB, posterior −5.25, lateral ±1.35, and ventral −3.4; ARC, posterior −1.45, lateral ±0.3, ventral −6.1. After an injection was completed, the pipette was left in place for five minutes before removal, and this process was repeated for other injection sites. After the injections were completed, the incision was closed using veterinary tissue adhesive (3M Vetbond). For optic fiber implantation, small holes were drilled and 200 μm core fiber optic cannulae with ceramic ferrules (RWD Life Science) were lowered into the PB (posterior, −5.25, lateral ±1.5, and ventral −3.1 from bregma). To secure the cannula, a mixture of dental acrylic and adhesive (dental cement) was then applied to cover the bottom of the ceramic ferrule and the entire exposed area of the skull, anchoring the fiber optic cannulae to the skull. Once the cement had hardened, a non-absorbable suture was placed at the back of the incision to tighten the skin around the cement. After removing the mouse from the stereotaxic frame, the cannula was capped to prevent debris from entering. After surgery, mice were injected with Meloxicam subcutaneously at a dose of 4mg/kg and placed on a 37°C heating pad until recovered.

AAV and retrograde tracer injections

For projection-specific sequencing experiments, AAVrg-hSyn-Cre (Addgene: 105553) or HSV-hEf1a-mCherry-IRES-Cre (Mass General Brigham Gene Delivery Technology Core; Dr. Rachael Neve) was injected into the thoracic spinal cord (200 nL/side) or parabrachial region (100 nL/side) of H2B-TRAP mice. Spinal cord retrograde tracing histology was performed by injecting wild-type mice with Fluoro-Gold (FG; Fluorochrome) into the thoracic spinal cord (200 nL/side). For Cre-dependent EGFP-L10a expression in PVH^{Mc4r} neurons, *Mc4r*-2a-Cre mice received injections of AAV5-EF1a-FLEX-EGFP-L10a (Addgene: 98747) into the PVH (100 nL/side). These same mice received cholera toxin subunit B (CTB; List Biological Laboratories: 104) injections into the PB (50 nL/side). AAVDJ-hSyn-DIO-EGFP-TeTxLC (ETH Zurich Viral Vector Facility: v322-5) or AAV8-hSyn-DIO-EGFP (control virus; Addgene: 50457) was used for chronic Cre-dependent neuronal silencing experiments via injections into the PVH of *Brs3*-IRES-Cre or wild-type mice (15 nL/side). For CRACM electrophysiology experiments, Cre-dependent AAV8-hSyn-DIO-mCherry (Addgene: 50459) was injected into the PVH (50 nL/side) and Flp-dependent AAV5-EF1a-fDIO-ChR2-eYFP (UNC viral vector core: 172055) was injected into the ARC (200 nL/side) of *Brs3*-IRES-Cre::*Npy*-IRES-Flp mice. *In vivo* optogenetic terminal stimulation experiments were done by injecting Cre-dependent AAV9-EF1a-DIO-ChR2-eYFP (Addgene: 20298) or AAV9-EF1a-DIO-ChR2-mCherry (Addgene: 20297) into the PVH (15 nL/side) of *Brs3*-IRES-Cre mice. Control virus for the optogenetic terminal stimulation experiments was Cre-dependent AAV8-hSyn-DIO-mCherry. Of note, one round of snRNA-seq with 10X Chromium was done by injecting the PVH (50 nL/side) of *Sim1*-Cre mice with AAVDJ-hSyn-DIO-H2B-mCherry (Boston Children's Hospital Viral Core)[107] and collecting mCherry-positive nuclei.[115,116] Also, the male mouse used for MERFISH Slide 3 was injected with AAVrg-hSyn-mCherry (Addgene: 114472) into the spinal cord (200 nL/side), and the male mouse used for MERFISH Slide 6 was injected with AAVrg-hSyn-mCherry into the parabrachial region (50 nL/side). After stereotactic injections, experiments were initiated three weeks post-surgery for all AAVs to allow for suitable expression levels. FG and CTB were injected 3–7 days before sacrifice to enable retrograde transport. All stereotaxic injection sites were validated by post hoc immunofluorescence. All "misses" or "partial" hits, as determined by fluorescent expression in the target cells, were excluded from data analysis.

RNAscope fluorescent *in situ* hybridization and immunofluorescence

RNAscope Multiplex Fluorescent Reagent Kit V2 (Advanced Cell Diagnostics: 323100) was used to perform *in situ* hybridization of mRNA in the PVH. For neuroendocrine PVH neuron labeling paired with FISH, adult mice aged 8–12 weeks were injected intraperitoneally with Fluoro-Gold (Fluorochrome; 30 mg/kg) one week prior to lethal injection of ketamine/xylazine (150mg/kg ketamine +15 mg/kg xylazine) and transcardial perfusion with RNase-free PBS and 10% phosphate-buffered formalin (Fisher: SF100-20). Brains were then extracted and post-fixed in 10% phosphate-buffered formalin overnight, followed by consecutive overnight incubations in 10%, 20%, and 30% RNase-free sucrose solution in PBS. Coronal brain sections were then sliced at 30 μm using a freezing microtome, briefly washed in RNase-free 0.5% Triton X-100 (Sigma Aldrich) in PBS, mounted onto Superfrost Plus slides, and stored at −80°C until ready for FISH. RNAscope was completed according to the manufacturer's protocol. First, the slides were removed from the freezer and washed with sterile PBS, followed by a 30-min incubation at 60°C. The slides were then fixed again with 10% phosphate-buffered formalin for 15 min at 4°C, followed by dehydration in 50%, 70%, and 100% ethanol solutions. Hydrogen Peroxide was then added to slides for 10 min at room temperature. After washing twice with PBS, a hydrophobic barrier surrounding the tissue sections was drawn on the slide (ImmEdge: H-4000), and the slide was treated with Protease III for 30 min. Slides were next hybridized with RNAscope probes targeting mRNA for genes of interest for two hours at 40°C, including *Aox3* (Mm-Aox3: 836451-C1), *Avp* (Mm-Avp: 401391-C3), *Brs3* (Mm-Brs3: 454111-C1 or C3), *Col12a1* (Mm-Col12a1: 312631-C2), *Crh* (Mm-Crh: 316091-C1), *Esr2* (Mm-Esr2: 316121-C3), *Nfix* (Mm-Nfix: 522331-C2), *Npr3* (Mm-Npr3: 502991-C2), *Npsr1* (Mm-Npsr1: 317501-C1), *Oxt* (Mm-Oxt: 493171-C2), *Pla2r1* (Mm-Pla2r1-No-XHs: 854581-C1), *Rxfp3* (Mm-Rxfp3: 439381-C1), *Scgn*

(Mm-Scgn: 482721-C2), *Sim2* (Mm-Sim2: 1108911-C1), *Sst* (Mm-Sst: 404631-C1), or *Trh* (Mm-Trh: 436811-C1). After hybridization, slides underwent three amplification steps at 40°C (AMP1-FL and AMP2-FL for 30 min each, AMP3-FL for 15 min), followed by probe-specific HRP amplification and Opal dye (Akoya Biosciences) incubations at 40°C for visualization. After the Opal dye step, HRP blocker was applied, and this process was repeated until all probes were developed.

After completing RNAscope slides were washed three times with PBS and incubated overnight at 4°C with primary antibody prepared in blocking solution made with PBS, 0.4% Triton X-100, and 3% normal donkey serum. The primary antibodies used include rabbit anti-Fluoro-Gold (1:300; Millipore Sigma: AB153-I), goat anti-cholera toxin subunit B (1:300: List Biological Laboratories: 703), and rabbit anti-GFP (1:1,000; Thermo Fisher Scientific: A-11122). The next day, slides were washed five times with PBS, and incubated for two hours at room temperature in the appropriate Alex Fluor-conjugated donkey secondary antibody (1:1,000; Thermo Fisher Scientific) prepared in blocking solution. Finally, slides were washed again three times with PBS before coverslipping with VECTASHIELD mounting media with DAPI (Vector Laboratories: H-1900-10). Slides were imaged at 10× magnification with an Olympus Slideview VS200 slide-scanning microscope or at 20× magnification with a Leica Stellaris 5 confocal microscope.

Histological analysis of Cre-reporters and immunofluorescent experiments

At the conclusion of experiments involving Cre-reporter expression, retrograde tracer injections, and AAV injections, brain/spinal cord histology was performed. For Cre-reporter histology, R26-LSL-EGFP-L10a reporter mice were crossed with *Slc17a6* (VGLUT2)-IRES-Cre, *Slc32a1* (VGAT)-IRES-Cre, and *Sim1*-Cre mice. Adult mice were lethally anesthetized and transcardially perfused as above. Brains were then extracted and postfixed overnight in 10% phosphate-buffered formalin. Brains were then sliced coronally at 40 μm and mounted directly onto glass slides. For experiments requiring immunofluorescence, floating sections were washed in PBS prior to incubation overnight at room temperature in primary antibody solution as described above. All primary antibodies used are described above, except rat anti-mCherry (1:3,000; Thermo Fisher Scientific: M11217). The next day, sections were washed and incubated with Alex Fluor-conjugated donkey secondary antibody as above. Subsequently, tissue was washed, mounted onto slides, and coverslipped with VECTASHIELD mounting media with DAPI. Slides were imaged at 10× magnification with an Olympus Slideview VS200 slide-scanning microscope.

Body weight measurements after PVH^{Brs3} neuron silencing

To begin bodyweight studies, initial body weights were recorded for littermate *Brs3*-IRES-Cre and wild-type mice, and mice were then divided into the stereotactic surgery groups described above (AAVDJ-hSyn-DIO-EGFP-TeTxLC or AAV8-hSyn-DIO-EGFP). Subsequently, mice remained group-housed for the duration of the experiment. Body weights were recorded during the light cycle between 10:00 a.m. and 12:00 p.m. every 7 days for a total of 6 weeks. At the end of the study, mice were transcardially perfused as above for histological analysis of AAV expression in the PVH. Mice without bilateral expression of GFP were removed from the analysis.

Channelrhodopsin-2 (ChR2)-assisted circuit mapping (CRACM)

Brs3-IRES-Cre::*Npy*-IRES-Flp mice underwent stereotactic surgery at 5–7 weeks old as described above, and CRACM experiments were completed at 8-10 weeks-old as described previously.[124] Briefly, mice were anesthetized with isoflurane, decapitated, and brains were rapidly extracted and submerged in ice-cold choline-based cutting solution saturated with carbogen (95% O_2, 5% CO_2). For slice preparation, brains were sliced at 300 μM coronally with a vibrotome (Campden 7000smz-2) and kept in cutting solution at 34°C for 10 min. Next, slices were transferred to oxygenated artificial cerebrospinal fluid (aCSF; 126 mM NaCl, 21.4 mM $NaHCO_3$, 2.5 mM KCl,1.2 mM NaH_2PO_4,1.2 mM $MgCl_2$, 2.4 mM $CaCl_2$, and 10 mM glucose) for at least 45 min at room temperature. After recovery, an individual coronal slice containing the PVH region was placed in a recording chamber where it was continuously superfused with oxygenated aCSF and viewed under a microscope (SliceScope Pro 1000, Scientifica). PVH^{Brs3} neurons were fluorescently labeled by Cre-dependent AAV-mCherry, and Flp-dependent AAV-ChR2-eYFP drove ChR2 expression in ARC$^{Npy/Agrp}$ neurons. Open-tip resistances for patch pipettes were 3–5 MΩ and were backfilled with CsCl internal solution: 140 mM CsCl, 1 mM BAPTA, 10 mM HEPES, 5 mM $MgCl_2$, 5 mM Mg-ATP, 0.3 mM Na_2GTP, and 10 mM lidocaine N-ethyl bromide (QX-314), adjusted to pH 7.35 with CsOH and an osmolarity of 290 mOsm. To assess connectivity between ARC$^{Npy/Agrp}$ → PVH^{Brs3} neurons, whole-cell voltage-clamp recordings from PVH^{Brs3} neurons were done while photostimulating ChR2-expressing terminals from ARC$^{Npy/Agrp}$ neurons. To evoke IPSCs with light, four 470 nm light pulses of 2 ms duration were administered one second apart during the first four seconds of a ten second protocol that was repeated 30 times. Blue light was applied via wide-field exposure through the 40× objective with an LED (Cool LED pE-100). The light output was controlled by a programmable pulse stimulator (Master 8, A.M.P.I.) and pClamp 10.5 software (Axon Instruments). Light-evoked IPSCs were isolated via glutamate receptor antagonism with 2 mM kynurenate, and short latency (≤6 ms) responses upon light stimulation were considered to be light-driven.

Food intake measurements after PVH^{Brs3} neuron → PB optogenetic stimulation

We assayed dark-cycle food intake while optogenetically stimulating PVH^{Brs3} neuron projections to the parabrachial region. *Brs3*-IRES-Cre mice underwent stereotactic surgery for AAV injections and optic fiber implants as described above. Prior to beginning optogenetics studies, mice were allowed to recover for at least three weeks and were acclimated to tethering to patch cords and single housing. On experimental days, patch cords were bilaterally attached to optic fibers over the PB two hours before the onset

of dark, and food was removed. Food was returned at the onset of dark and intake was then measured every hour for the first three hours of the dark cycle. Trials consisted of a baseline light-off tests, followed by light-stimulation experimental trials on the following day. Photostimulation was delivered with square wave pulses of 473 nm blue light, delivered at ~8–10 mW of power measured at the fiber tip, with 20 Hz stimulation (10ms pulses; 2 s on, 3 s off). LabView software and a National Instruments NIDAQ board were used to control our stimulation protocol.

QUANTIFICATION AND STATISTICAL ANALYSIS

Quantification of PVH neuroendocrine neurons

For each neuroendocrine subtype, 12 images (for *Crh*, *Trh* and *Sst*) and 8 images (for *Avp* and *Oxt*) covering rostral to caudal PVH, were exported using QuPath[109] from the RNAscope and ip Fluoro-Gold labeling experiments (Figures 1K–1P), which consisted of three channels: Fluoro-Gold, the neuroendocrine hormone of interest, and a marker gene for the corresponding neuroendocrine subtype identified by sc/snRNA-seq. Neuroendocrine peptide gene-positive cells were identified using the Cellpose2 model ("cyto2"), with manual adjustments made for any misidentified or missed cells. The selected cell masks were saved and imported into Fiji (ImageJ),[110] where the multi-point tool further facilitated counting of neurons expressing neuroendocrine marker gene pairs (*Crh-Scgn*, *Trh-Nfix*, *Sst-Col12a1*, *Avp-Pla2r1*, and *Oxt-Rxfp3*) and whether they were labeled by Fluoro-Gold. The percentage of FG-positive neurons for each neuroendocrine marker gene pair was then calculated. The same method is applied to count FG-negative neurons that expressed neuroendocrine peptide genes (FG-negative *Crh*, *Trh*, *Sst*, *Avp* and *Oxt*) and whether they co-expressed the associated neuroendocrine marker gene identified by sc/snRNA-seq.

Statistical analysis

Statistics for sc/snRNA-seq and MERFISH were performed in R, as described above. All other analyses were conducted using GraphPad Prism (v10.3.0), with the specific statistical tests for each experiment indicated in the figure legends. No statistical methods were used to predetermine sample size, and randomization and/or blinding were not applied for sc/snRNA-seq or MERFISH experiments. Randomization was applied for body weight and food intake experiments. For body weight gain measurements, a two-tailed one-way ANOVA followed by Tukey's post hoc test was used. For the optogenetic feeding behavior assay, a two-tailed two-way repeated measures ANOVA with virus and laser as factors was performed, followed by Sidak's post hoc multiple comparisons test. All results are presented as mean ± SEM. Statistical significance was defined as $p < 0.05$, with asterisks indicating significance levels: $^{*}p < 0.05$, $^{**}p < 0.01$, and $^{****}p < 0.0001$.